Scaling Laws for the Heterogeneously Heated Free Convective Boundary Layer

CHIEL C. VAN HEERWAARDEN, JUAN PEDRO MELLADO, AND ALBERTO DE LOZAR

Max Planck Institute for Meteorology, Hamburg, Germany

ABSTRACT

The heterogeneously heated free convective boundary layer (CBL) is investigated by means of dimensional analysis and results from large-eddy simulations (LES) and direct numerical simulations (DNS). The investigated physical model is a CBL that forms in a linearly stratified atmosphere heated from the surface by square patches with a high surface buoyancy flux. Each simulation has been run long enough to show the formation of a peak in kinetic energy, corresponding to the ''optimal'' heterogeneity size with strong secondary circulations, and the subsequent transition into a horizontally homogeneous CBL.

Scaling laws for the time of the optimal state and transition and for the vertically integrated kinetic energy (KE) have been developed. The laws show that the optimal state and transition do not occur at a fixed ratio of the heterogeneity size to the CBL height. Instead, these occur at a higher ratio for simulations with increasing heterogeneity sizes because of the development of structures in the downward-moving air that grow faster than the CBL thickness. The moment of occurrence of the optimal state and transition are strongly related to the heterogeneity amplitude: stronger amplitudes result in an earlier optimal state and a later transition. Furthermore, a decrease in patch size combined with a compensating increase in patch surface buoyancy flux to maintain the energy input results in decreasing KE and a later transition. The simulations suggest that a CBL with a heterogeneity size smaller than the initial CBL height has less entrainment than a horizontally homogeneous CBL, whereas one with a larger heterogeneity size has more.

1. Introduction

When the surface is warmer than its overlying stably stratified atmosphere, a convective boundary layer (CBL) forms in which rising plumes mix the air. Most of the knowledge of CBLs is acquired by studying this layer over a spatially homogeneous land surface (e.g., Deardorff 1970; Tennekes 1973; Kaimal et al. 1976; Lenschow and Stankov 1986; Fedorovich 1995; Jonker et al. 1999; Garcia and Mellado 2014). In reality, however, the heating of the atmosphere is often heterogeneous, for instance because of variations in land cover, topography, and soil moisture.

Mahrt (2000) classified heterogeneities into three regimes, based on the height at which the influence of heterogeneity vanishes: in the microscale regime, the influence of the heterogeneities vanishes below the surface layer, and the CBL behaves as if it were a horizontally homogeneous one. The effects of heterogeneities in the macroscale regime extend beyond the boundary layer; that is, the size of heterogeneity is so large that a heterogeneous CBL develops that scales with its corresponding local surface properties. In between those, we find the mesoscale regime, in which the heterogeneities alter the characteristics of the turbulence in the CBL to such an extent that the classical scaling laws are no longer applicable.

Before going into more detail on mesoscale heterogeneities, we define three properties of heterogeneity that we use throughout this paper: the heterogeneity size, which is the size of an entire sequence of a warm patch and its colder surroundings; the patch size, which is the size of the warm region; and the heterogeneity amplitude, which is the surface buoyancy flux difference between the patch and its surroundings (see section 2).

The heterogeneously heated CBL in the mesoscale regime has been studied from observations (e.g., Kang et al. 2007; Górska et al. 2008; Prueger et al. 2012) and has been the subject of many large-eddy simulation (LES) studies. In the latter, notably the influences of heterogeneity size and amplitude, but also of wind speed

Corresponding author address: Chiel C. van Heerwaarden, Max Planck Institute for Meteorology, Bundesstrasse 53, 20146, Hamburg, Germany.
E-mail: chiel.vanheerwaarden@mpimet.mpg.de

and orientation, have been studied (e.g., Avissar and Schmidt 1998; Albertson and Parlange 1999; Raasch and Harbusch 2001; Patton et al. 2005; Esau 2007; van Heerwaarden and Vilà-Guerau de Arellano 2008; Kang 2009; Kang and Lenschow 2014; Maronga and Raasch 2013; Sühring and Raasch 2013). The most important conclusion to be drawn from those studies is that there is an optimal heterogeneity size with respect to the CBL height that triggers the strongest circulations, which result in a peak in the vertically integrated kinetic energy (KE). This size has been identified as 4–9 times the height of the CBL (Patton et al. 2005). Furthermore, several studies (Avissar and Schmidt 1998; Patton et al. 2005; van Heerwaarden and Vilà-Guerau de Arellano 2008) have shown an increase of the circulation strength with increasing heterogeneity amplitude. The exact properties of the optimal state, however, are still unknown. It is unclear to which extent there is a relationship between the optimal heterogeneity size and the heterogeneity amplitude. Furthermore, the exact boundary between mesoscale and microscale heterogeneity remains unknown.

This paper aims at studying transient cases in which a convective boundary layer evolves through the regimes we explained above and eventually forms a horizontally homogeneous CBL. Our specific objective is the development of scaling laws for the properties of the optimal state and the transition from the meso- to the microscale regime. To do this, we have created an idealized system that consists of a stable linearly stratified atmosphere heated from the surface by square patches. On this system we have applied dimensional analysis, in order to derive parameterizations of relevant properties (see section 2). Variation of the nondimensional parameters describing the heterogeneity geometry and amplitude allows for a wide range of surface conditions. By creating patches that occupy half of the surface area, one can, for instance, construct a structure that resembles the chessboard-like patterns used in many LES studies (e.g., Raasch and Harbusch 2001; Courault et al. 2007), but it is also possible to create isolated plumes over each patch (Morton et al. 1956). In our idealized system, we consider simple heterogeneity shapes. There has been a trend to study the complex geometry of realistic surface forcings (e.g., Huang and Margulis 2009; Shao et al. 2013; Sühring and Raasch 2013), but we have chosen to first try to understand the basic aspects of the transient system with idealized heterogeneity shapes. In the conclusions of our paper, we discuss how our results could be extended to more complex cases.

To derive the aforementioned scaling laws, we have done numerical simulations of the transient system described above. The temporal development of a heterogeneously heated CBL has implicitly been addressed by studies that impose a diurnal cycle to the model (Huang and Margulis 2010; Maronga and Raasch 2013), but we have chosen a simpler approach and impose a constant surface buoyancy flux. We do this by starting the simulation under the condition that the heterogeneity regime classifies as either macro- or mesoscale. We continue the simulation until the integral length scale of the CBL has grown so far beyond that of the heterogeneity at the surface that the CBL transitions to the microscale regime. Our simulations consist of a combination of LES and direct numerical simulations (DNS) (see section 3). LES has been used because it opens the possibility of studying a large parameter space, and it has been proven useful for studying the heterogeneously heated CBL. For simulations with very small patches and relatively high fluxes, we have performed DNS in order to circumvent potential problems with the sensitivity of narrow plumes to the subgrid constants (Yan 2007) and with the validity of surface layer similarity due to the very large horizontal buoyancy gradients at the surface. Although surface models have been applied locally or with limited averaging (Bou-Zeid et al. 2005), we have decided not to push the surface model to the limit for the cases with very small patches and have opted for DNS. In the appendix, we show a brief comparison between DNS and LES. A more complete discussion on surface models is found in Piomelli and Balaras (2002), Brasseur and Wei (2010), and Shao et al. (2013).

Even though we have achieved moderate convective Reynolds numbers (~5000), Garcia and Mellado (2014) show Reynolds number similarity for the bulk statistics of the CBL at comparable values. We assume that the independence applies to heterogeneity as well, since the secondary circulations, which are the most pronounced effects of heterogeneity, manifest themselves at spatial scales comparable to the CBL height.

We have conducted two experiments (see section 3). The first experiment is used to study the importance of heterogeneity size and amplitude, based on a surface buoyancy flux pattern with equal area coverage for patch and nonpatch regions. We have performed a sensitivity study on the heterogeneity size for three different amplitudes. In the second experiment, we have investigated the influence of the patch size on the transition between the mesoscale and microscale regimes. We have done a series of simulations in which, for a given reference CBL height, the heterogeneity size and the mean surface buoyancy flux is constant, but with a decreasing patch size and increasing patch heat flux for the different simulations.

The results of these two experiments are discussed in sections 4, 5, and 6. We present a more detailed

interpretation of the time evolution by means of conditional statistics in section 7. In section 8, we develop the scaling laws. Subsequently, we discuss the conditions of the optimal state and the enhancement of entrainment compared to previous studies in section 9 and end with the conclusions in section 10.

2. Theory

a. Classification of heterogeneity

In this study, we consider surface heterogeneity that consists of an array of identical elements. Each element has a warm square patch with a size X_P and a total heterogeneity size X_H (Fig. 1). The characteristic length scale of the turbulence is L. Based on these three length scales, we can create a two-dimensional space that spans the axes X_H/L, the heterogeneity size parameter, and X_P/L, the patch size parameter (Fig. 2). Note that the locations in this parameter space are so far qualitative, as they depend on the exact definition of L, which is still unknown, as our analysis has to deliver it. Within this parameter space, we find the horizontally homogeneous convective boundary layer when $X_P/L = X_H/L > 0$; that is, where the patch covers the entire heterogeneity length (Fig. 1). As soon as we move away from this line, we enter into the classification regimes introduced by Mahrt (2000). Under the condition $X_H/L > X_P/L \gg 1$, we find the macroscale regime, with large patches that contain their own isolated CBL. When $X_P/L < X_H/L \ll 1$, the heterogeneity is small compared to the integral length scale of the turbulence, and we retrieve the microscale regime. Then the heterogeneity reduces to roughness elements, and the CBL properties scale as those of the horizontally homogeneous one. The remaining classifiable regime is that in which $X_H/L \gtrsim 1$ and $X_P/L \lesssim 1$; that is, in which the heterogeneity size is at least of the same order of magnitude as the integral length scale of the turbulence, whereas the patch size is equal to or smaller than this length scale. Here, we find the mesoscale regime. In this regime, each patch supports its own plume, which may or may not interact with those of neighboring patches. Under the condition that $X_P/L \ll 1$ and $X_H/L \gg 1$, the patch reduces to an isolated point source and we find the isolated plume in a stratified atmosphere (Morton et al. 1956).

This classification does not take into account the heterogeneity amplitude, which is the difference in surface buoyancy flux between the patch and the nonpatch area, and assumes that all flux is located over the patch. We will show in section 5 that the inclusion of a flux in the nonpatch region does not change the regimes, but instead shifts their boundaries within the parameter space.
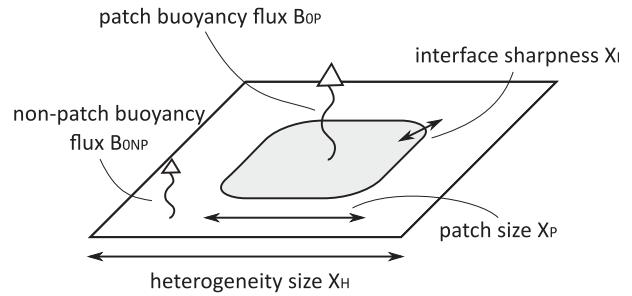

FIG. 1. Schematic view of a surface heterogeneity element. The surface of the physical model consists of an array of these elements in both horizontal directions.

b. Nondimensionalization of the idealized system

Our idealized system consists of a stably stratified atmosphere heated from the surface by square patches, which can be described by nine parameters:

$$(\nu, \kappa, N^2, X_H, X_P, X_I, B_0, B_{0NP}, B_{0P}). \qquad (1)$$

Here, the stratified atmosphere is characterized by its viscosity ν (m^2 s^{-1}), thermal diffusivity κ (m^2 s^{-1}), and the buoyancy lapse rate N^2 (s^{-2}) that defines the linear stratification. These parameters show that our system is defined on the basis of buoyancy $b \equiv (g/\theta_0)(\theta - \theta_0)$ (m s^{-2}). This has the advantage that one loses the temperature dimension, and it makes the results applicable to any buoyancy-driven system.

The surface (Fig. 1) is described by the surface buoyancy flux of the patches B_{0P} (m^2 s^{-3}) and of the nonpatch regions B_{0NP} (m^2 s^{-3}), the patch size X_P (m), the heterogeneity size X_H (m), and the width of the interface between the patch and the nonpatch region X_I (m). The following relationship links the mean surface buoyancy flux B_0 (m^2 s^{-3}) to that of the patches and allows for the elimination of the parameter B_{0P} from the system:

$$B_0 X_H^2 = B_{0NP}(X_H^2 - X_P^2) + B_{0P} X_P^2. \qquad (2)$$

With length and time as the two basic dimensions of the parameters in our system, the eight remaining parameters can be combined into six nondimensional groups:

$$\left(\frac{\nu}{\kappa}, \frac{L_0}{\eta}, \frac{X_H}{L_0}, \frac{B_{0NP}}{B_0}, \frac{X_P}{X_H}, \frac{X_I}{L_0} \right), \qquad (3)$$

where we have introduced two new length scales L_0 and η. The first length scale L_0 is a reference Ozmidov length (e.g., Smyth and Moum 2000):

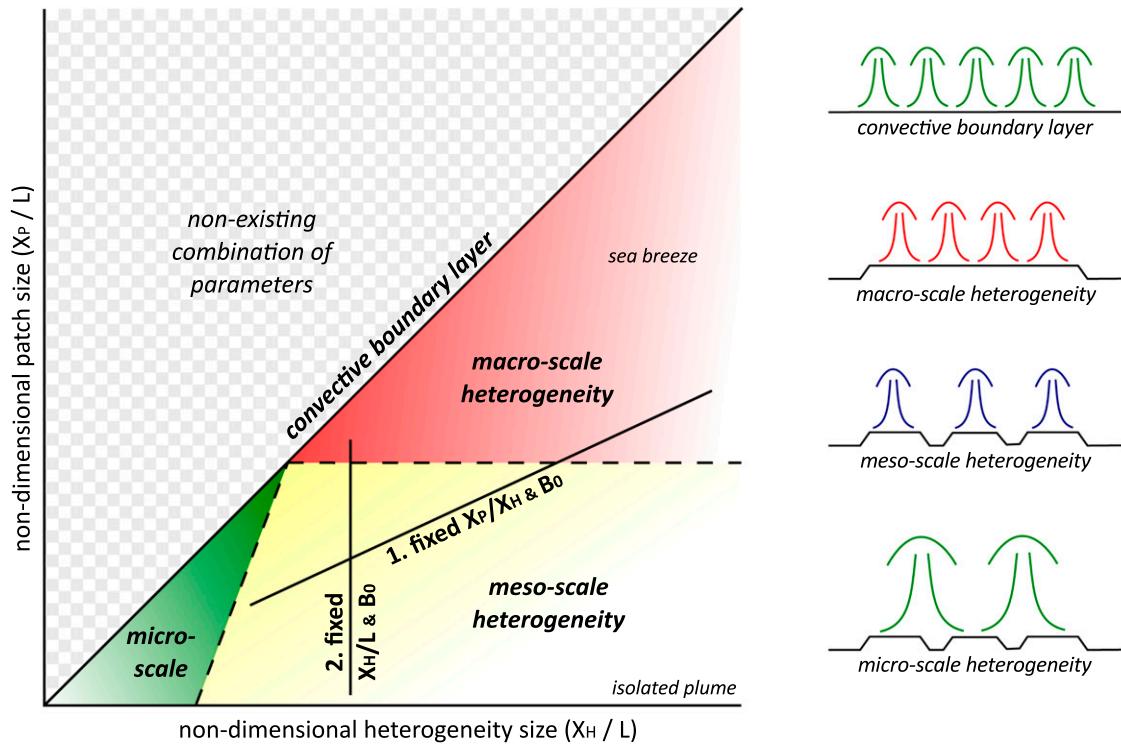$$L_0 = \left(\frac{B_0}{N^3} \right)^{1/2}, \qquad (4)$$

FIG. 2. Schematic view of the parameter space and the defined regimes. The two numbered thick lines represent the starting points of the simulations in the two experiments: The first diagonally through the parameter space at a constant patch size parameter X_P/X_H, and the second vertically at a constant heterogeneity size parameter X_H/L_0.

which can be interpreted as a reference height for the initial CBL, where "reference" implies that the actual initial height will be this quantity multiplied with an arbitrary constant of order one. Note that the original definition of the Ozmidov length is $(N^3/\epsilon)^{1/2}$. In a purely convective flow, the dissipation ϵ can be substituted with the buoyancy flux B_0 because of the approximate balance between the buoyancy flux and dissipation (Garcia and Mellado 2014). The second length scale η is a reference Kolmogorov length $\eta = (\nu^3/B_0)^{1/4}$.

The six nondimensional parameters can be interpreted as follows:

ν/κ is the Prandtl number.

L_0/η is the ratio of the reference initial CBL height scale to the reference Kolmogorov length scale and is related to a convective Reynolds number: $\mathrm{Re} = B_0/(N^2\nu) = (L_0/\eta)^{4/3}$.

X_H/L_0 is the heterogeneity size parameter. It is the ratio of the heterogeneity size to the reference initial CBL height. It is a measure of the degree of interaction between adjacent patches.

$B_{0\mathrm{NP}}/B_0$ is the heterogeneity amplitude parameter. It is the ratio of the buoyancy flux of the nonpatch area to the mean surface flux. It is a measure of the heterogeneity amplitude: the larger this number, the

the lower the amplitude. The value varies between 0 and 1. We chose this parameter instead of B_{0P}/B_0, because it explicitly measures the flux that enters in between the patches. A change in B_{0P}/B_0, on the other hand, could also be the result of a change in patch size X_P.

X_P/X_H is the patch size parameter. Its square measures the ratio of surface area coverage patches X_P^2 to the total area X_H^2 within a heterogeneity element. It varies between 0 and 1. When multiplied with X_H/L_0, X_P/L_0 is recovered, which can be interpreted as the number of plumes per patch (see Fig. 2).

X_I/L_0 is the ratio of the width of the interface between the patch and the environment to the reference initial CBL height; thus, it measures the interface sharpness.

Our set of nondimensional parameters yields a six-dimensional parameter space. We reduce the degrees of freedom of the study by making three additional assumptions. First, we assume the Prandtl number ν/κ to be unity. This allows for simpler wall scalings (Mellado 2012), but the influence of difference between the atmospheric value of 0.71 and unity are negligible in the flow characteristics (Ahlers et al. 2009). Second, by using the highest achievable resolution within our

computational possibilities, we maximize L_0/η to get the highest possible scale separation and thus Reynolds number. For LES, the scale separation can be quantified based on the effective Reynolds number that is a function of the eddy viscosity (Sullivan and Patton 2011). A detailed discussion on the chosen resolution is found in section 3. Third, we assume the interface between the patch and nonpatch areas X_I/L_0 to be small and constant (0.05 m for DNS; 1 m for LES).

To conclude, the set of parameters that we study is

$$\left(\frac{X_H}{L_0}, \frac{B_{0NP}}{B_0}, \frac{X_P}{X_H}\right). \qquad (5)$$

All of our simulated cases have a unique value within this parameter space. Note that these parameters are used in combination with actual time and length scales, which we define next, in order to scale the results later on.

c. Normalization of the results

In the results (see sections 4 and 5), we study the influence of heterogeneous heating in terms of a deviation from the horizontally homogeneous CBL. Many of the bulk statistics of this CBL become self-similar (Garcia and Mellado 2014). These statistics can be described using the height coordinate z combined with the length scale h_{enc} and the velocity scale w_{enc}, which has the same form as Deardorff's velocity scale:

$$h_{enc} = \left(\frac{2B_0}{N^2}t\right)^{1/2}; \qquad (6)$$

$$w_{enc} = (B_0 h_{enc})^{1/3}. \qquad (7)$$

The encroachment height h_{enc} is the height that the CBL achieves under conditions of growth by heating against the stratified atmosphere. It is the analytical solution of the mixed-layer equations with only encroachment driving the growth $[dh_{enc}/dt = B_0/(N^2 h_{enc})]$. The ratio of the CBL height h to h_{enc} becomes constant in time for the self-similar horizontally homogeneous CBL and is 1.23 in case the height of the maximum buoyancy gradient is chosen as the definition for h (Garcia and Mellado 2014). Any deviation from this height can therefore be interpreted as the influence of heterogeneity.

Since the height scale h_{enc} is a function of time only, it can be used as a replacement for time in the analysis of the results, and the nondimensional time evolution can be expressed in terms of h_{enc}/L_0. This scaled coordinate unifies simulations with different mean surface buoyancy fluxes and lapse rates, as these are contained in L_0. Therefore, it facilitates the derivation of general scaling

laws pursued in this study, and it aids the combination of DNS and LES results. The ratio h_{enc}/L_0 is equal to $(2tN)^{1/2}$ and is thus proportional to the square root of the nondimensional time tN.

The common measure to scale heterogeneities, the ratio X_H/h, can therefore be written in terms of the heterogeneity size X_H/L_0 and the time coordinate h_{enc}/L_0 as follows: $X_H/h = (1/1.23)(X_H/L_0)(h_{enc}/L_0)^{-1}$.

3. Methods

a. Formulation and model description

The system is described in terms of the time-varying velocity vector with components u_i and buoyancy b with the Boussinesq approximation applied. In the LES, filtered equations are solved in the inviscid form, with a subfilter-scale model that takes into account the subfilter-scale fluxes.

The velocity boundary conditions are set as no penetration ($w = 0$) and no slip ($u = v = 0$) at the bottom boundary and no penetration and free slip $[(\partial u/\partial z) = (\partial v/\partial z) = 0]$ at the top boundary. The buoyancy flux at the surface B_0 has a spatial pattern that can be described by a sequence of error functions that is controlled by the parameters B_{0NP}, B_{0P}, X_H, X_P, and X_I, where B_{0P} is acquired through Eq. (2). The surface area is divided into L_x/X_H by L_y/X_H heterogeneity elements (Fig. 1), where the domain size (L_x, L_y) is always an integer multiple of X_H. Within each heterogeneity element, where we assume that x and y vary between 0 and X_H, the local surface buoyancy flux B_S is calculated as

$$\alpha(x') = \frac{1}{2} - \frac{1}{2}\text{erf}\left(2\frac{|2x' - X_H| - X_P}{X_I}\right); \qquad (8)$$

$$B_S(x, y) = B_{0NP} + (B_{0P} - B_{0NP})\alpha(x)\alpha(y), \qquad (9)$$

where we use an error function to describe the transition between patch and nonpatch areas.

The top boundary condition for buoyancy is a fixed gradient that corresponds to the stratification of the free atmosphere N^2. The initial fields for velocity are set to zero, whereas the initial buoyancy profile is zero at the surface and increases with a constant gradient N^2 with height. Random noise is superimposed on the velocity fields in order to provide the perturbations that eventually lead to convection. The noise exponentially decays with height and is negligible beyond $4L_0$.

In this study we make use of the MicroHH code (https://github.com/microhh), which is a 2D parallel combined DNS–LES code. To solve the governing equations, fully conservative finite-difference schemes (Morinishi et al. 1998; Vasilyev 2000) have been used,

TABLE 1. Overview of the LES used in experiment 1. The values L_x, L_z, N_x, and N_z are the domain sizes and grid points in the horizontal and vertical directions. In our experiments, B_0 and L_0 have the values of $2.393 \times 10^{-3}\,\mathrm{m^2\,s^{-3}}$ and 49.6 m. The area ratio X_P^2/X_H^2 is fixed at 0.5.

Label	X_H (m)	X_P (m)	X_H/L_0	X_P/L_0	B_{0P}/B_0	B_{0NP}/B_0	L_x (m)	L_z (m)	N_x	N_z	Run (h)
CBL	—	—	—	—	—	—	12 000	6000	1024	768	24.0
L0250_0.0	250	176.8	5.0	3.6	2.0	0.0	3000	3000	384	384	4.0
L0500_0.0	500	353.6	10.1	7.1	2.0	0.0	3000	3000	512	384	9.0
L1000_0.0	1000	707.1	20.2	14.3	2.0	0.0	8000	5000	768	640	15.0
L2000_0.0	2000	1414.2	40.3	28.5	2.0	0.0	8000	5000	768	640	25.0
L0250_0.4	250	176.8	5.0	3.6	1.6	0.4	3000	3000	384	384	2.6
L0500_0.4	500	353.6	10.1	7.1	1.6	0.4	3000	3000	384	384	6.0
L1000_0.4	1000	707.1	20.1	14.3	1.6	0.4	5000	3000	512	384	14.0
L2000_0.4	2000	1414.2	40.3	28.5	1.6	0.4	8000	4000	768	512	18.0
L3000_0.4	3000	2121.3	60.5	42.8	1.6	0.4	9000	4000	768	512	20.0
L4000_0.4	4000	2828.4	80.6	57.0	1.6	0.4	12 000	4000	1152	512	32.0
L6000_0.4	6000	4242.7	121.0	85.5	1.6	0.4	18 000	6000	1536	768	51.0
L0250_0.8	250	176.8	5.0	3.6	1.2	0.8	3000	3000	384	384	3.0
L0500_0.8	500	353.6	10.1	7.1	1.2	0.8	3000	3000	384	384	3.0
L1000_0.8	1000	707.1	20.1	14.3	1.2	0.8	5000	3000	512	384	4.2
L2000_0.8	2000	1414.2	40.3	28.5	1.2	0.8	8000	4000	768	512	15.0
L4000_0.8	4000	2828.4	80.6	57.0	1.2	0.8	12 000	4000	1152	512	19.0

with second-order accuracy for the LES and fourth-order for the DNS. These are combined with a low-storage third-order Runge–Kutta time integration scheme (Williamson 1980). The pressure is acquired by solving a Poisson equation. Here, the horizontal dimensions are decoupled using a Fourier decomposition such that, for each mode, a tridiagonal (LES) or heptadiagonal (DNS) matrix has to be solved. In the top of the domain (upper 25%) a sponge layer is applied that prevents the reflection of gravity waves back into the domain with a damping time scale that is infinity at the height where the sponge layer starts and exponentially decreases to $N/(2\pi)\,\mathrm{s}^{-1}$ at the top of the domain. In case of LES the no-slip condition at the surface is imposed through a surface model based on Monin–Obukhov similarity theory (MOST). The subfilter-scale fluxes are calculated following the Smagorinsky–Lilly model with wall damping near the surface and in which MOST is used to calculate the mean strain rate near the wall. The surface and subfilter-scale model are similar to those in the Dutch Atmospheric Large-Eddy Simulation (DALES), and a description can be found in Heus et al. (2010).

b. Numerical experiments

In our first experiment, we simulate a heterogeneity that resembles the chessboard pattern by having $X_P^2/X_H^2 = 0.5$. We have simulated the growth of the CBL over this configuration for different heterogeneity size parameters X_H/L_0 and heterogeneity amplitude parameters B_{0NP}/B_0 (thick line number 1 in Fig. 2). The setup of our LES is based on the free-convection case

from Conzemius and Fedorovich (2006), but with a reduced mean surface buoyancy flux B_0 such that the shared parameters among all simulations are a B_0 of $2.393 \times 10^{-3}\,\mathrm{m^2\,s^{-3}}$ (corresponding to a virtual temperature flux of $0.0732\,\mathrm{K\,m\,s^{-1}}$) and a lapse rate N^2 of $9.81 \times 10^{-5}\,\mathrm{s^{-2}}$ (equal to $0.003\,\mathrm{K\,m^{-1}}$), which results in an L_0 of 49.6 m. The surface model uses a roughness length of 0.1 m, and the subfilter-scale model uses a Smagorinsky constant of 0.21.

Table 1 lists the conducted LES in this experiment. We span heterogeneity sizes ranging from 250 to 6000 m, and three different variations of the heterogeneity amplitude B_{0NP}/B_0. In the table, we also show the nondimensional numbers that we use later for creating the scaling laws for these experiments. We have labeled the simulations based on their heterogeneity size and the heterogeneity amplitude. We have chosen a grid spacing of 7.8 m for the cases with small patches, and we relax the horizontal resolution to a maximum of 10.4 m for the largest patches. Sullivan and Patton (2011) have shown that beyond their $(256)^3$ case, which has a grid spacing of $20 \times 20 \times 8\,\mathrm{m}^3$, the bulk statistics of the CBL converge. If we take into account that our chosen resolution is finer than theirs and that heterogeneity manifests itself in the larger spatial scales, our numerical setup is adequate.

In the second experiment (thick line number 2 in Fig. 2), we study the importance of the patch size by varying the parameter X_P/X_H, while keeping the heterogeneity size parameter X_H/L_0 constant and the flux of the nonpatch area B_{0NP} at zero. Table 2 lists the properties of the simulations performed in this

TABLE 2. As in Table 1, but for the DNS used in experiment 2 with B_0 and L_0 having the values of $3.2 \times 10^{-3}\,\mathrm{m^2\,s^{-3}}$ and 0.0248 m.

Label	X_H (m)	X_P (m)	X_H/L_0	X_P/L_0	B_{0P}/B_0	B_{0NP}/B_0	L_x (m)	L_z (m)	N_x	N_z	Run (s)
D0.125_S	0.125	0.0707	5.0	2.8	3.125	0.0	1.0	1.38	1024	1024	73.9
D0.125_M	0.125	0.0884	5.0	3.6	2.000	0.0	1.0	1.38	1024	1024	55.3
D0.125_L	0.125	0.1000	5.0	4.0	1.563	0.0	1.0	1.38	1024	1024	45.7
D1.000_0.4	1.000	0.7071	40.3	28.5	1.600	0.4	2.0	1.38	2048	1024	109.9

experiment. All three simulations have a mean surface buoyancy flux B_0 of $3.2 \times 10^{-3}\,\mathrm{m^2\,s^{-3}}$ and a lapse rate N^2 of $3\,\mathrm{s^{-2}}$, which gives an L_0 of 0.0248 m. The suffixes S, M, and L in the labels refer to small, medium, and large patch size parameters X_P/L_0, and suffix 0.4 refers to the heterogeneity amplitude. The chosen grid spacing in the DNS experiments relies on the resolution study of Garcia and Mellado (2014). We have increased the grid resolution compared to this study to take into account that we use explicit fourth-order spatial schemes, in contrast to their compact schemes. To allow for a comparison, we have made simulation D0.125_M equal to L0250_0.0 in terms of nondimensional parameters. In addition, we have performed simulation D1.000_0.4, which has the same nondimensional parameters as L2000_0.4. In the appendix, we show a short comparison between DNS and LES.

4. Illustration of optimal-state formation and transition

We start the analysis of our results with a visual description of the two main phenomena that we focus on in this paper: the formation of a peak in KE that represents the optimal heterogeneity state and the transition from the mesoscale to the microscale regimes.

We have chosen one of the cases with relatively large patches (D1.000_0.4) with respect to the initial integral length scale of the plumes in order to demonstrate the onset and decay of the optimal state (Figs. 3a–c). In Fig. 3a, we find that each patch initially supports more than one rising plume. One could therefore argue that the system is in transition between the macro- and mesoscale. There is an overturning circulation at the sides of each patch that almost extends to the surface. This circulation tries to bring in all small plumes that originate at the surface into the adjacent large structure. In the region near the CBL top, lateral spread of a plume occurs very fast (Baines and Turner 1969; Cardoso and Woods 1993) such that the entire region in between the plumes is part of the downward flow from the beginning. As soon as the CBL has grown so large that the plumes merge into a single one, while the overturning circulation still exists, we enter the optimal state in which the

KE peaks (Fig. 3b). Typical features here are a well-defined peak in the boundary layer height above the patches, combined with strong entrainment events near the side of the plumes (van Heerwaarden and Vilà-Guerau de Arellano 2008; Ouwersloot et al. 2011; Sühring et al. 2014) and a circulation that has enough horizontal space to not mix with the circulation of the adjacent patch. After the optimal state (Fig. 3c), the CBL grows so high that the overturning circulation is no longer able to reach the surface. Instead, the horizontal motions near the top of the CBL collide with those of neighboring thermals.

While only the systems with relatively large heterogeneity sizes go through the steps we described above, each simulation eventually contains a transition from the meso- to the microscale regimes. We show this transition in Figs. 3d–f. Here, we have selected simulation D0.125_M, because we did not run D1.000_0.4 until transition. Furthermore, the simulations without flux in nonpatch regions have, as we show later, the strongest transitions and are therefore most suited for visualization of the transition.

Far before the transition (Fig. 3d) the plumes extend over the entire height of the CBL such that eight distinct structures are visible almost until the interface between the CBL and the free atmosphere. While time progresses and the CBL grows, the turbulence in the upper regions increases and disturbs the plumes such that their signature starts to be lost at the top of the CBL (Fig. 3e). We identify this moment with the onset of the transition, which announces itself in the merging of several of the plumes with their neighbors. The end state of the simulation is the CBL in the microscale, where rising plumes are supported by multiple patches (Fig. 3f).

The time evolution of the simulations toward transition can also be shown in a more quantitative way using ensemble averages. Figure 4 shows the mean plume, acquired from averaging cross sections through the center of the patch, parallel to either the x or the y axis. This results in two cross sections per plume, thus 128 in total for simulation D0.125_M, as there are 64 plumes. The cross sections are made at four instants: during the optimal state (Fig. 4a), in between the optimal state and transition (Fig. 4b), right before transition (Fig. 4c), and after transition (Fig. 4d).
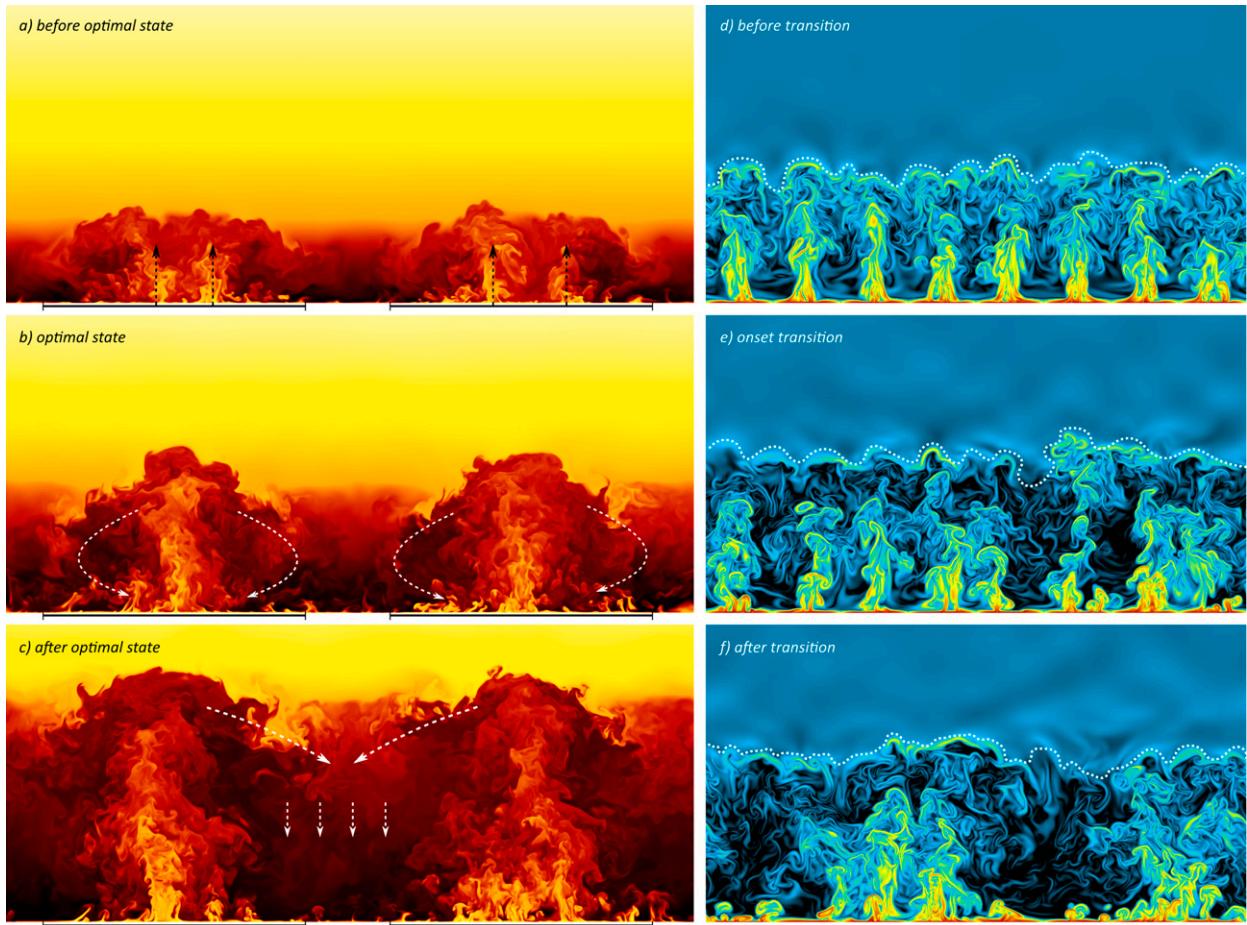
FIG. 3. Vertical cross sections depicting the formation of the optimal state and the transition from the meso- to the microscale regimes. (a)–(c) The buoyancy taken from simulation D1.000_0.4 at different stages in the evolution during the mesoscale regime. (d)–(f) The logarithm of the length of the buoyancy gradient vector at different stages during the transition taken from simulation D0125_M. All cross sections are taken such that they cut through the center of a row of patches. In (a)–(c), the patches are marked below the panels. In (a), the dotted arrows represent the rising plumes. In (b) and (c), the dotted arrows represent the extent and nature of the circulation. In (d)–(f), the interface between the CBL and the free atmosphere is indicated with a white dotted line. Both color scales are nonlinear and are chosen to display the turbulent structures the best.

Figure 4a shows that during the peak the highest scaled vertical velocities are reached at $z/h_{enc} = 0.7$, with a large part of the plume exceeding a value of 1.5. At the same time, the stable stratification that surrounds the plumes is preserved. As time progresses, the inversion strengthens, and the stable stratification in between the plumes is gradually broken down (see Fig. 4b). The maximum velocity is now reached closer to the surface at $z/h_{enc} = 0.5$. Figure 4c shows that right before transition, the CBL is almost well mixed, and the stable stratification has nearly vanished. The maximum velocity is found now at $z/h_{enc} = 0.4$, at which the horizontally homogeneous CBL also has its maximum (see Fig. 5). After transition (Fig. 4d), the plumes are no longer visible,

but the buoyancy displays a blending region that extends up to $0.2(z/h_{enc})$, in which the influence of the patch is still visible.

5. The influence of heterogeneity size and heterogeneity amplitude

a. Simulations without flux in between the patches

We start the quantitative analysis with the results of our first experiment, where we have studied the importance of the heterogeneity size parameter X_H/L_0 and heterogeneity amplitude B_{0NP}/B_0, under a constant patch area coverage X_P^2/X_H^2. A short overview of the X_H/h ratio at the optimal state and transition and simulation
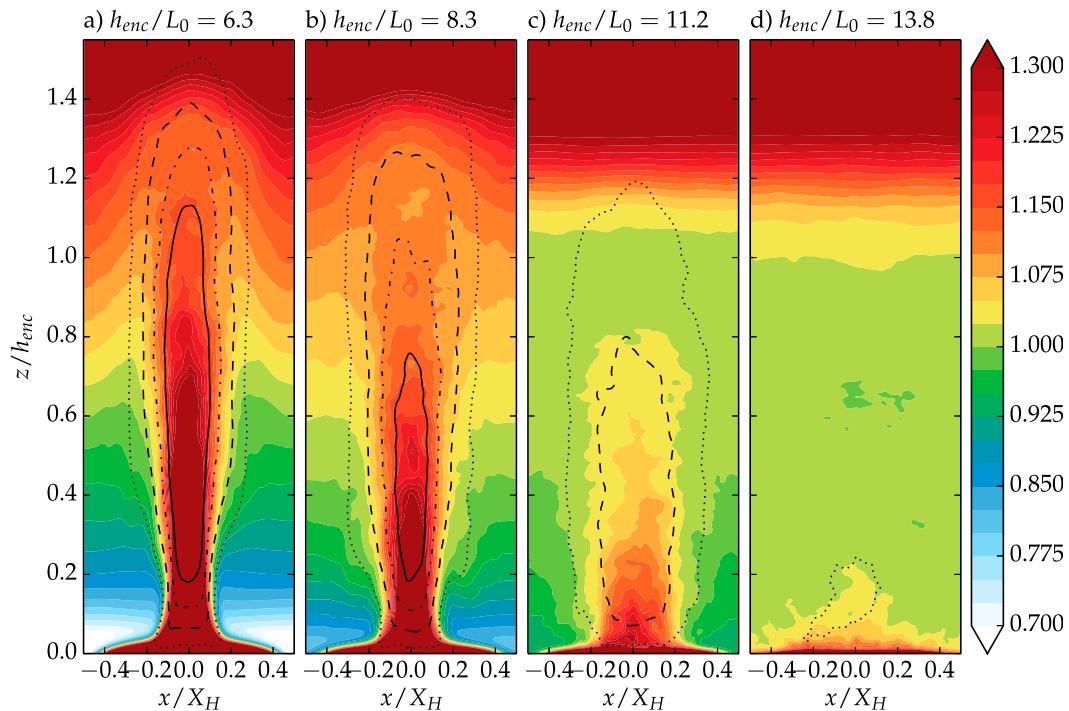
FIG. 4. Vertical cross sections of ensemble averages of buoyancy b normalized by $h_{enc}N^2$ (shades) and vertical velocity w normalized by w_{enc} [contour lines indicate 0.1 (dotted), 0.5 (dashed), 1.0 (dashed–dotted), and 1.5 (solid)] for simulation D0.125_M. (a)–(d) h_{enc}/L_0 = 6.3, 8.3, 11.2, and 13.8.

duration to get there are given in Table 3. We analyze first the results of the simulations that have no fluxes in between the patches ($B_{0NP}/B_0 = 0$) in order to understand the system in its most basic form.

We have chosen to base our analysis on the vertically integrated KE (denoted as $\langle KE \rangle$) and on the CBL height h of the simulations (Fig. 5). The KE contains a very clear signal of heterogeneity (Avissar and Schmidt 1998; Letzel and Raasch 2003; Patton et al. 2005) and is therefore a good indicator for the occurrence of the optimal state and the transition. The boundary layer height is chosen, because in the homogeneously heated CBL, the ratio h/h_{enc} quickly becomes constant. Therefore, the deviation of this ratio from that of the homogeneously heated CBL is another good proxy for the effects of heterogeneity, especially with respect to the question of whether the heterogeneity modifies the entrainment process. The time axes of our figures are expressed in the nondimensional unit h_{enc}/L_0, which defines the scale separation between the height of the boundary layer and the initial reference length L_0 (see section 2c). In all figures belonging to this experiment, the line colors represent the heterogeneity amplitude.

Figure 5a contains the time evolution of the vertically integrated KE. Each simulation shows a peak in KE

near $5(h_{enc}/L_0)$ that marginally moves forward in time for the simulations with a larger heterogeneity size. The magnitude of the peak in KE, at a value of approximately $0.68(h_{enc}w_{enc}^2)$, is insensitive to the heterogeneity size. During the time period in which the peak occurs, the KE is larger than that of the horizontally homogeneous CBL during the same stretch of time. This implies that the heterogeneity imposes a strong circulation to the system, which, in this stage, enhances the integrated KE beyond that of the reference CBL. Patton et al. (2005) found an enhancement of more than 20%, whereas Letzel and Raasch (2003) found under certain conditions a doubling of the kinetic energy. Our heterogeneity amplitude resembles more those of Letzel and Raasch (2003); therefore, our enhancement of KE in the peak is in a similar range. We, however, do not observe under any conditions the oscillations that Letzel and Raasch (2003) and Kang (2009) find and believe that these are the result of their initial temperature profile.

Our findings should be interpreted with care, because in this experiment the peak falls in the initial transient of the simulation. For the horizontally homogeneous CBL, it takes at least (5 to 8) × (h_{enc}/L_0) until the self-similar state for the boundary layer height has been reached. This corresponds to a height in the range of 300–500 m
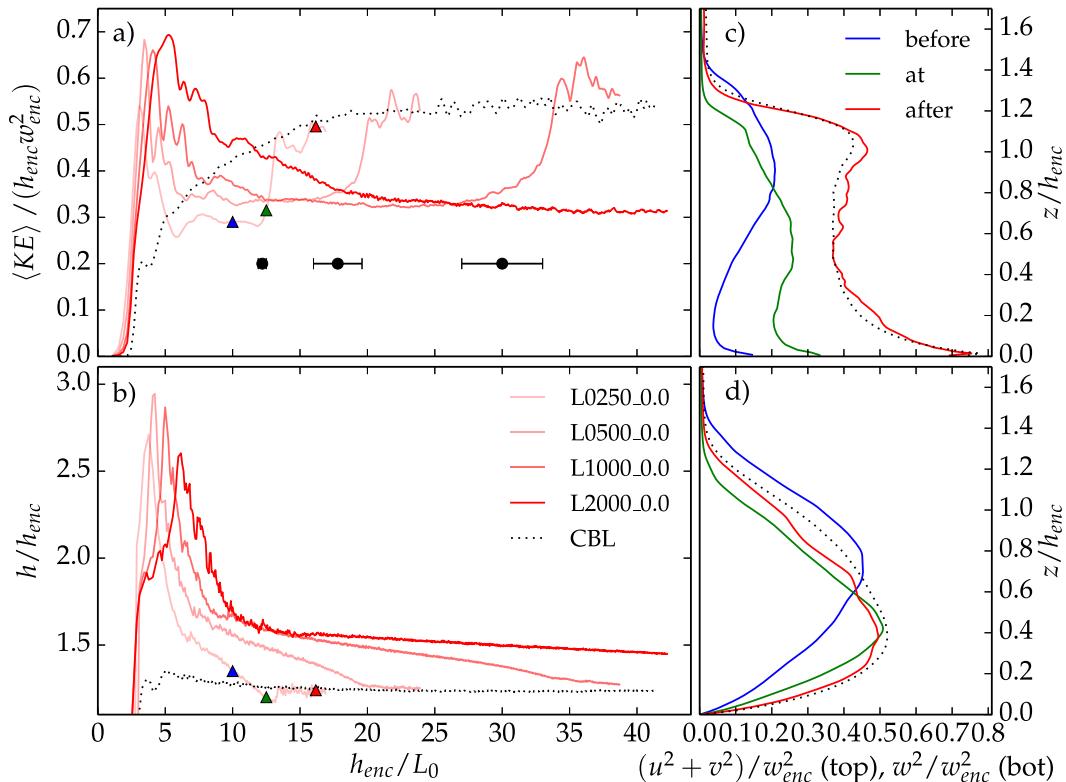
FIG. 5. Time evolutions of the (a) vertically integrated KE and (b) CBL height for simulations with $B_{0NP} = 0$. Three colored triangles on the graph of simulation L0250_0.0 mark the moments that correspond to the three vertical profiles of (c) horizontal velocity variance and (d) vertical velocity variance. These triangles also mark the time instants at which cross sections in Figs. 3d–f are taken. The dots mark the transition from the meso- to the microscale regime.

for a CBL with an $L_0 \sim 50$ m, reached after 30 min–1 h. From now on, we take this as the minimum scale separation between h_{enc} and L_0 required for drawing conclusions on the behavior of the optimal state. Note that this transient has a clear physical meaning, as it denotes the transition from a growing boundary layer that does not feel stratification and therefore grows proportional to $t^{3/2}$ (Mellado 2012) to a CBL that feels its overlying stratification.

After having the peak in KE, we enter an intermediate phase that eventually leads to the transition from meso- to microscale heterogeneity. During this phase, the KE falls to a value that is constant under convective scaling (i.e., a quasi-steady state). While the achieved KE is the same, the time it takes to reach it is progressively longer for larger heterogeneity sizes. The magnitude of approximately $0.33(h_{enc}w_{enc}^2)$ is the same for all cases, except for simulation L0250_0.0 with the smallest heterogeneity size. This simulation reaches quasi-steady state at a slightly lower value, which we attribute to the fact that the quasi-steady state is reached in the very early stage of the initial transient, before $5(h_{enc}/L_0)$.

In the intermediate phase, the normalized KE level (0.33) falls below that of the horizontally homogeneous CBL (0.55). This is an important finding, because it indicates that the heterogeneity no longer enhances the KE, but instead suppresses it. The system is now constrained in developing larger spatial scales by the fact that the plumes cannot increase their size, because the pattern of their surface energy input is fixed, whereas in the horizontally homogeneous CBL, the surface area that feeds the large plumes has a persistent growth in time.

The eventual transition into a horizontally homogeneous CBL is represented by the sudden increase in KE back to the levels of the horizontally homogeneous CBL. The moments of the transition are marked explicitly in Fig. 5, where the error bars indicate the period during which the transition occurs and the dot is taken as the middle of this range. The time at which the transition occurs does not correspond to a fixed ratio of h_{enc} to X_H, which is the multiplication of h_{enc}/L_0 and the reciprocal of the heterogeneity size $(X_H/L_0)^{-1}$. Instead, for larger heterogeneity sizes, the transition occurs progressively earlier. For instance, L0250_0.0 initiates the transition

TABLE 3. Overview of the main results of the LES belonging to experiment 1. The quantity $(X_H/h)_P$ is the ratio of the heterogeneity size to the CBL height at the optimal state, The term $(X_H/h)_T$ is the ratio of the heterogeneity size to the CBL height at the transition, T_P is the elapsed time in hours at the moment of the optimal state, and T_T is the elapsed time in hours at the moment of transition.

Label	$(X_H/h)_P$	$(X_H/h)_T$	T_P (h)	T_T (h)
CBL	—	—	—	—
L0250_0.0	—	0.33	—	2.1
L0500_0.0	—	0.46	—	4.4
L1000_0.0	—	0.54	—	12.6
L2000_0.0	—	—	—	>26
L0250_0.4	1.3	0.50	0.14	0.9
L0500_0.4	2.2	0.70	0.20	1.9
L1000_0.4	3.8	0.89	0.25	4.7
L2000_0.4	4.9	1.25	0.63	9.6
L3000_0.4	6.1	1.42	0.90	16.9
L4000_0.4	7.5	1.44	1.06	29.0
L6000_0.4	8.5	1.65	1.95	50.0
L0250_0.8	0.2	—	0.17	—
L0500_0.8	1.9	—	0.26	—
L1000_0.8	2.2	—	0.77	—
L2000_0.8	3.1	—	1.58	—
L4000_0.8	4.3	—	3.28	—

at a ratio of $2.4(h_{enc}/X_H)$ whereas L1000_0.0 starts its transition already at $1.5(h_{enc}/X_H)$. Note that we could not run simulation L2000_0.0 to transition because of the constraining domain size. Table 3 shows us that even for the smallest case, it takes at least 2 h to go into transition, for L1000_0.0 it takes more than 12 h, and the largest case does not even reach transition within 26 h. Our results show that, for this heterogeneity amplitude, heterogeneity sizes beyond 1000-m size will not go into transition during a typical day.

To understand the transition in more detail, Figs. 5c and 5d show the development of the vertical profiles of horizontal and vertical velocity variances before, during, and after the transition. The profiles corroborate our findings discussed before. Before the transition, the horizontal velocity variance is locked at a low value, compared to a horizontally homogeneous CBL, with the most distinct difference near the surface. Here, the horizontal motions are only representing the neck formation of the plumes (Fig. 3d), resulting in a normalized KE of 0.15, 5 times smaller than that of a horizontally homogeneous CBL. At the same time, the vertical velocity variance is distributed over height differently. As soon as the plumes start to merge (Fig. 3e), the horizontal velocity variance rapidly increases near the surface as the horizontal motions extend now over multiple patches. After the transition, the statistics have nearly converged to those of the horizontally homogeneous CBL.

The evolution through the different stages described above is also reflected in the evolution of the CBL height

(Fig. 5b). As explained in section 2c, all CBL heights h hereafter are the height of the mean maximum gradient. In case of a horizontally homogeneous CBL, normalization of the height with h_{enc} results in a constant value in time of 1.23 (see section 2c). There is a distinct peak in the height at the same time of the maximum KE, occurring at low values of h_{enc}/L_0. The magnitude of the peak is decreasing with increasing heterogeneity size, from $3.0(h/h_{enc})$ to $2.5(h/h_{enc})$. The period during which the optimal state evolves toward the quasi-steady state consists of two phases: first, there is a sharp decrease phase, for instance between $7(h_{enc}/L_0)$ and $10(h_{enc}/L_0)$ for L2000_0.0, with approximately the same decrease rate for all cases; and, second, it is superseded by a period in which the slope of the line gradually becomes constant.

During this period, the height decreases toward that of the horizontally homogeneous CBL. The fact that the excess height with respect to the reference CBL decreases in time is illustrated well by the cross sections in Fig. 3. In the beginning, the plumes can rise relatively undisturbed, which allows them to reach a large height. Later, the upper part of the CBL gets more disturbed, preventing the plumes from reaching their undisturbed height more and more. As soon as the transition starts, the reduction in excess height accelerates, for instance, seen at $30(h_{enc}/L_0)$ in L1000_0.0, where the transition quickly breaks down the one-plume-per-patch structure. Ultimately, the simulation follows the reference line of the horizontally homogeneous CBL after completing the transition. In section 9, we discuss this finding with respect to the question of whether entrainment is modified by heterogeneity.

b. Simulations with a flux in between the patches

Introducing a flux in between the patches ($B_{0NP}/B_0 > 0$) alters the flow considerably. Figure 6 shows the time evolution of vertically integrated KE and vertical profiles of velocity variance. For this experiment, we leave the discussion of the height evolution to section 8, since the application of the scaling laws allow for an easier interpretation of this variable. Figure 6a shows the time evolution of the KE for all cases with a B_{0NP}/B_0 ratio of 0.4, where 80% of the energy input is at the patches and 20% is in between them.

We find that inserting a flux in nonpatch areas results in a system that delays the formation of the optimal state compared to cases without a flux and has increasing KE values with increasing heterogeneity sizes. If we again consider those cases that have their peak in KE beyond $5(h_{enc}/L_0)$, then we find the instant of the optimal state increasing from approximately $7(h_{enc}/L_0)$ in simulation L2000_0.4 to $12(h_{enc}/L_0)$ in simulation L6000_0.4, whereas the normalized KE increases from 0.58 to 0.7,
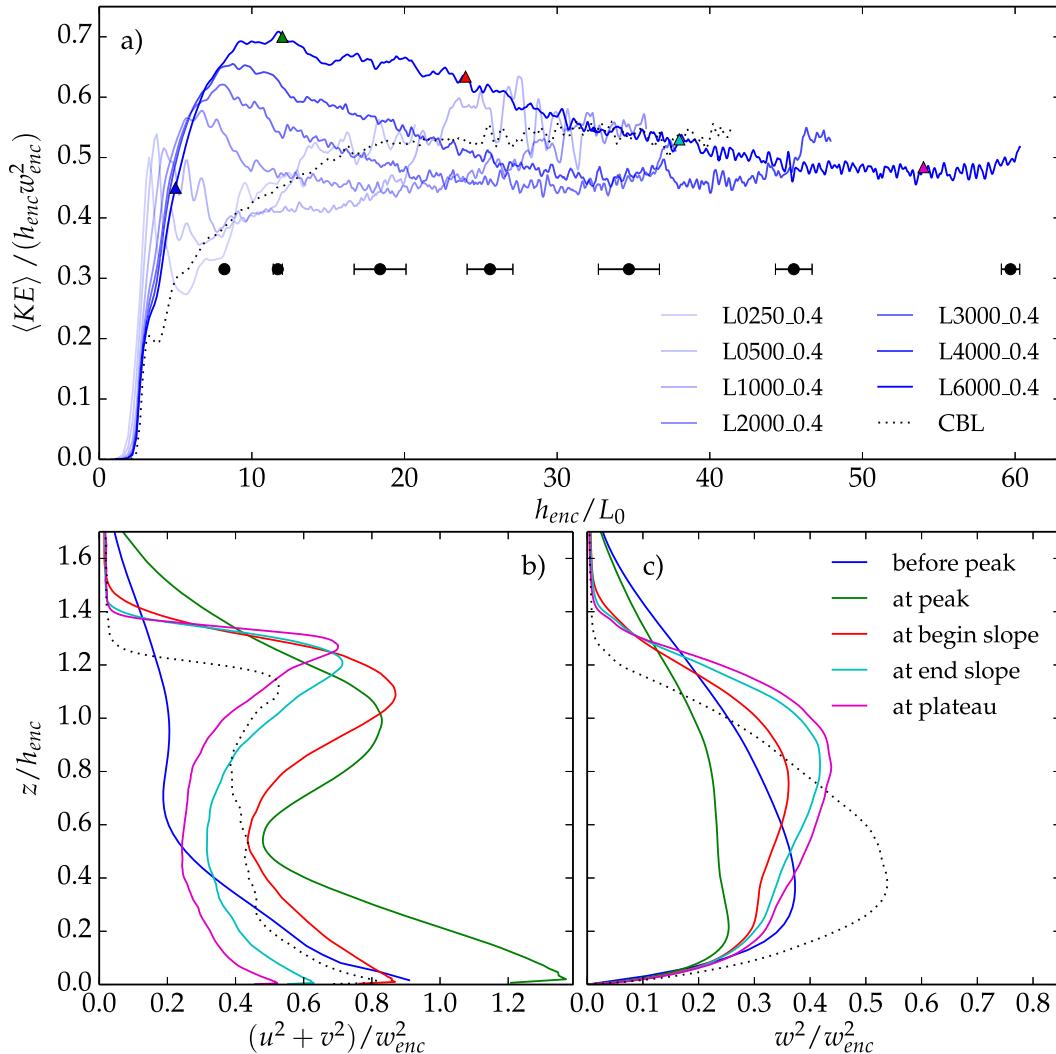
FIG. 6. (a) Time evolution of the vertically integrated KE for the cases with a flux in between the patches, described by parameter $B_{0NP}/B_0 = 0.4$. Five colored triangles on the graph of simulation L6000_0.4 mark the time instants that correspond to the vertical profiles of (b) horizontal velocity variance and (c) vertical velocity variance. The dots in (a) mark the transition from the meso- to the microscale regime.

respectively. In dimensional units (see Table 3), this corresponds to the optimal state at a CBL height of 410 m after approximately 40 min in case of L2000_0.4, whereas L6000_0.4 has its peak at a CBL height of 705 m, after 2 h of growth. The value of h_{enc}/L_0 at which the peak occurs is thus a function of the heterogeneity amplitude B_{0NP}/B_0. We take these findings into account in our scaling laws (see section 8). Again, we find that in the peaks the KE is almost a factor of 2 larger than in the case of a horizontally homogeneous CBL, thereby exceeding the enhancement that Patton et al. (2005) found, because we have a larger heterogeneity amplitude.

The decay phase after the optimal state has a similar pattern as the simulations without flux in between the

patches, with a decrease in KE until an intermediate phase with constant normalized KE is reached at a magnitude of 0.45. This magnitude is lower than that of the CBL (0.55) but higher than the 0.33 found in Fig. 5. For the largest heterogeneity size L6000_0.4, the decay phase takes until $50(h_{enc}/L_0)$, because the system has to recover from a high peak in KE. In terms of typical atmospheric conditions (see Table 3), this corresponds to a height of approximately 3000 m, reached after 36 h. This duration is far beyond the duration of a day and is, therefore, not expected to occur in reality. This is an important finding, because it shows that, in the absence of wind (also for lower-amplitude cases), it is unlikely that the effects of large-scale heterogeneity vanish during one day.

In the presence of a flux in the nonpatch area, the system remains only shortly in its quasi-steady state before going into transition. For instance, simulation L1000_0.4 remains there approximately 5 units of h_{enc}/L_0, whereas simulation L1000_0.0, which has the same heterogeneity size, is able to remain there 3 times longer (Fig. 5a). In addition, the transitions occur relatively early compared to those with B_{0NP}/B_0 and the same spatial size in Fig. 5a.

Not only the transitions, but also the optimal states happen at a progressively lower value of h_{enc}/X_H. For instance, the transition of simulation L0500_0.4 occurs at a value of 1.2, whereas in case of L6000_0.4, the value is only 0.5. Since the progressively lower ratios are consistent among all results so far, we draw the conclusion that there must be a length or velocity scale in the system that grows faster than the CBL itself that is necessary for scaling the time evolution of the simulation. Hence, our results until here provide evidence that the ratio X_H/h, which has been widely used for identification of the optimal heterogeneity size, is not the appropriate one for expressing the state of the system.

To further illustrate the time evolution, we have plotted vertical profiles of velocity variances at five distinct moments (Figs. 6b–c) corresponding to the colored markers in Fig. 6a. At the peak, we find the typical velocity profiles that correspond to a heterogeneously heated CBL with secondary circulation, with strong peaks in the normalized horizontal velocity variance near the surface and near the top of the CBL (Avissar and Schmidt 1998; Patton et al. 2005). In decay phase, these peaks are still present (red line) but already lower near the surface (0.85) than during the peak (1.35). This process continues with a stronger reduction of both peaks (cyan line) ending up in the quasi-steady state (magenta line). The figure shows that during this transition, the KE gradually reduces below that of the reference CBL, although the peaks near the CBL top always remain higher.

6. The influence of the patch size

In our second experiment, we vary the patch size parameter X_P/X_H, while keeping the heterogeneity size parameter X_H/L_0 constant and the heterogeneity amplitude parameter B_{0NP}/B_0 equal to zero. By doing so, we complete the study of the parameter space [Eq. (5)], albeit only for the limiting case without surface flux in between the patches. Within this setup, a decrease in X_P/X_H automatically results in an increase in the patch heat flux B_{0P}. We focus on the approach of the transition and the transition itself, because the optimal state occurs in the initial transient (see section 5).

The vertically integrated KE evolution (see Fig. 7) shows that each of the simulations reproduces the intermediate state in KE followed by a transition, as in the simulations in the first experiment. Here, we find that a decrease in the patch size parameter X_P/X_H results in a lower integrated KE in the intermediate state, where D0.125_L has a normalized integrated KE of 0.3 and D0.125_S only reaches 0.2. At the same time, a smaller patch size implies a later transition, with the transitions ranging from $10.5(h_{enc}/L_0)$ for D0.125_L to $14.6(h_{enc}/L_0)$ for D0.125_S. The results suggest that smaller patches with a higher surface flux produce stronger plumes that delay the transition, because these are harder to break down. At the same time, even though the plumes are stronger, they fill up a smaller part of the domain, resulting in a lower integrated KE. Hence, an increase in patch buoyancy flux due to a reduction in X_P/X_H is not able to compensate for the loss in surface area.

The time evolution of the CBL height (Fig. 7b) indicates that a higher surface flux over a smaller patch results in a higher CBL, which decays at the same rate in time and in all simulations. We find, for instance, that all simulations start their linear decay at $5(h_{enc}/L_0)$. At this time, D0.125_S has an h/h_{enc} of 2 that leads to a transition at $14.4(h_{enc}/L_0)$, whereas D0.125_L starts at h/h_{enc} of 1.6, leading to a transition at $10(h_{enc}/L_0)$. The fact that the slope of the height evolution is the same in all cases suggests that the patch size X_P/X_H is not important in determining at which rate the plume structure is broken down. Instead, it is related to the heterogeneity size X_H/L_0, since B_{0NP}/B_0, our third parameter, is zero in this series of experiments.

7. Conditional statistics

To improve our understanding of the evolution of the system toward transition, we make use of conditional statistics. We have chosen two criteria for the conditioning, one based on whether we are above the patch $[B_S(x, y) \geq B_0]$ or not, and another based on the direction of the vertical velocity, to separate regions of upward and of downward-moving air.

Figure 8 shows the time evolution of the vertically integrated KE, where the line representing the total is identical to the L1000_0.0 line in Fig. 5a. We have selected simulation L1000_0.0 to illustrate the outcome of the conditional statistics, but the same interpretation can be made for the other simulations.

The lines of patch and nonpatch, and that of updraft and downdraft, add up to the total if they are weighted with their corresponding volume fractions. The patch produces more KE than the nonpatch region, because the plume is located here. Interestingly, the KE in the upward-moving air is higher $[\sim 0.9(h_{enc}w_{enc}^2)]$ than that
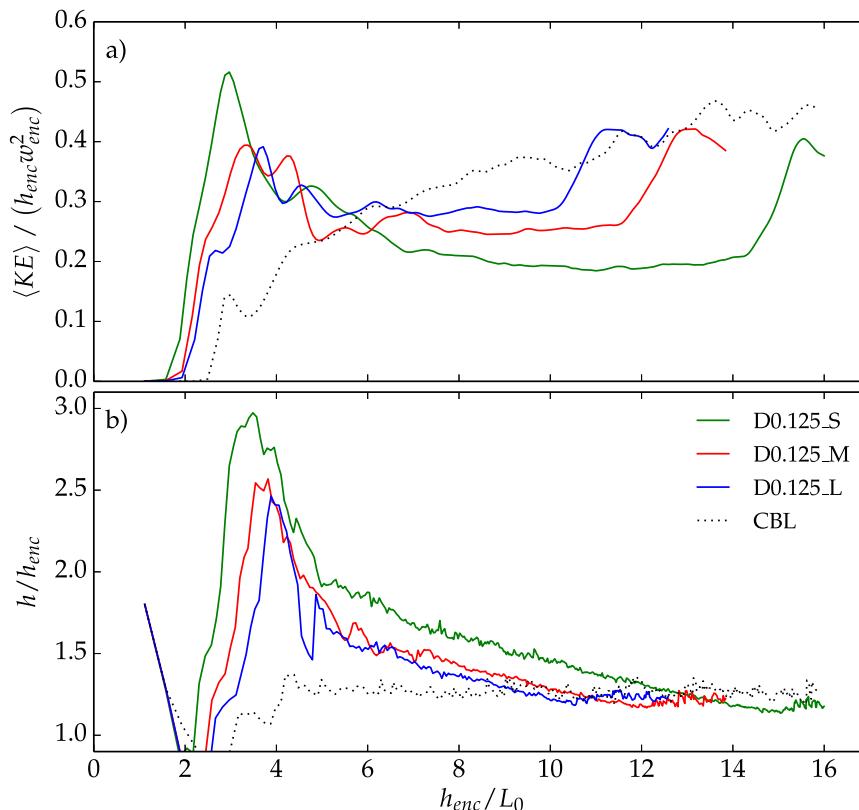
FIG. 7. Time evolutions of (a) the vertically integrated KE and (b) the boundary layer height for the DNS in the second experiment in which the patch size parameter X_P/X_H is varied.

over the patch [$\sim 0.6(h_{enc}w_{enc}^2)$]; thus, even though the plume area covers a large part of the patch (not shown), there is a significant contribution of less energetic downward-moving air to its KE. The figure shows that all components except that of the KE in the surroundings become approximately constant under convective scaling within the interval $h_{enc}/L_0 \sim 10-25$.

The steadily increasing KE over the nonpatch areas under a constant normalized KE explains partly the mechanisms driving the transition: An increasing KE over the nonpatch area implies that the energy in the downward motions, which remains constant, is first mostly contained over the patch but gradually occupies the entire area in between the plumes. As soon as the magnitudes of the KE of the nonpatch areas and the downward motions are equal, transition is triggered. To corroborate this, we have created a horizontal cross section of the variance contribution of the downward velocities at the beginning and the end of the phase in which the KE associated with the downward-moving air is constant under convective scaling (Fig. 9). The figure confirms our explanation, because it shows that initially the KE in the downward motions is produced in a narrow shell surrounding the plumes (Fig. 9a), and later

large structures occupy the entire area in between the plumes (Fig. 9b). These structures push the plumes so far out of their centerlines that they merge with adjacent plumes, thereby initiating transition.

8. Scaling laws

a. Development of scaling laws

Based on the results presented in the previous sections, we propose two scaling laws. The first is for the time evolution of our simulations and is valid for all our simulations, whereas the second concerns the magnitude of the KE for the simulations that have no flux in between the patches ($B_{0NP}/B_0 = 0$).

1) CHARACTERISTIC TIME SCALE

The main idea behind the scaling law for the time coordinate is that a plume is a three-dimensional structure that expands proportionally to the height of the CBL in all dimensions. By doing so, it fills up the space that surrounds the plumes, until the growing structures are so large, that they no longer fit within the heterogeneity size X_H/L_0. As soon as this happens, the transition from the meso- to microscale regime is triggered.
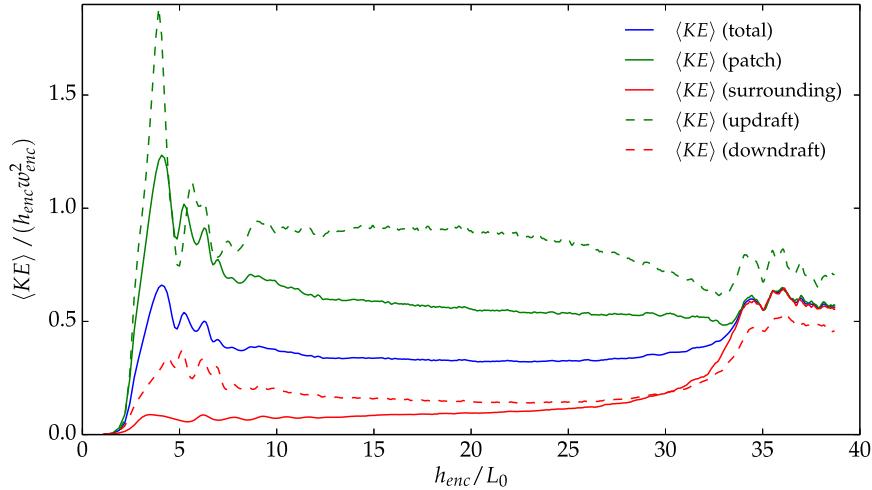
FIG. 8. Time evolution of the vertically integrated KE of case L1000_0.0, corresponding to different sampling conditions.

We assume that the initial radius R_0 of the plume, which consists of an upward plume and a downward shell, is proportional to X_P. It expands in time proportional to h_{enc} so that the horizontal area of the plume structure can be written as

$$\pi(R_0 + \alpha h_{enc})^2 \approx \pi R_0^2 + 2\pi \alpha R_0 h_{enc} \propto X_P^2 + 2\alpha X_P h_{enc}, \tag{10}$$

where α is a constant describing the expansion speed in the horizontal directions. The approximation in the second step is based on the assumption that the initial

plume radius R_0 is large compared to the added radius αh_{enc}. Figure 3a corroborates this assumption, as it shows that the structures occupy a large part of the total horizontal area. Our statistics show that area covered by updrafts is approximately constant in time and only increases right before transition such that the added area $2\alpha X_P h_{enc}$ consists of downdrafts only in the mesoscale regime. In addition, if we assume that the initial area is mostly covered by the updrafts in the plume, whereas the downdrafts are mostly in the added area, then the relative area coverage by downdrafts A_D/X_H^2 is proportional to
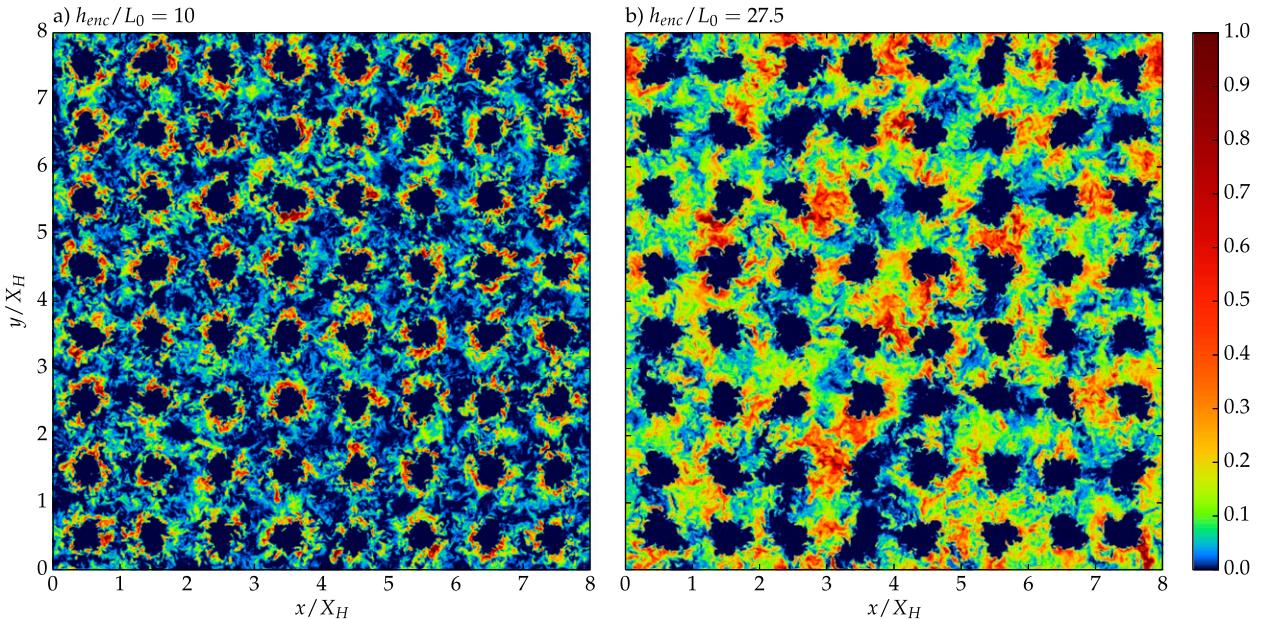

FIG. 9. Horizontal cross sections of the squared value of the downward velocity in simulation L1000_0.0 at a height of $4L_0$ taken at (a) $h_{enc}/L_0 = 10$ and (b) $h_{enc}/L_0 = 27.5$. Both states have the same $\langle KE \rangle$(downdraft)$/(w_{enc}^2 h_{enc})$ (see Fig. 8), but the pattern is clearly different.

$$\left(\frac{2\alpha X_P h_{\mathrm{enc}}}{X_H^2}\right) = 2\alpha\left(\frac{h_{\mathrm{enc}}}{L_0}\right)\left(\frac{X_P}{X_H}\right)\left(\frac{X_H}{L_0}\right)^{-1}. \quad (11)$$

If α were independent of any nondimensional parameter, then systems that vary only in their heterogeneity length would scale under h_{enc}/X_H. However, we do not observe that, and in order to scale the timing of the optimal state and the transition observed in Figs. 5 and 6, α appears to be related to the heterogeneity length X_H/L_0 as

$$\alpha \propto \left(\frac{X_H}{L_0}\right)^{1/3}, \quad (12)$$

so A_D/X_H^2 is proportional to $(X_H/L_0)^{-2/3}$. The interpretation of this dependence of α on the heterogeneity size is that the system organizes differently in the vicinity of neighboring patches; therefore, it is only valid in the mesoscale regime. In contrast to the horizontally homogeneous CBL, the system cannot expand freely but instead has to find its way around neighboring plumes. Our results suggest that this promotes the development of larger scales, but the exact mechanism is unclear.

To demonstrate that Eq. (12) is robust, we have created Fig. 10 based on the simulations in the first experiment. In this figure, we show the moment of the optimal state $(h_{\mathrm{enc}}/L_0)_P$ and transition $(h_{\mathrm{enc}}/L_0)_T$ as a function of the heterogeneity size X_H/L_0. The time instants of the transitions are taken from Figs. 5a and 6a, whereas the time instants of the peaks correspond to the moments of maximum vertically integrated KE (see Figs. 6 and 14). We can conclude from the figure that our proposed expression for α works in nearly the entire parameter space, except for the points that have a $(h_{\mathrm{enc}}/L_0)_P$ ratio less than 5, because the optimal state occurs in the initial transient of the simulation. Note that the peaks of the experiments with $B_{0\mathrm{NP}}/B_0 = 0$ are all below this ratio and are therefore not included in the figure.

Now, we can define the relative area coverage A_D/X_H^2 of the large structures in the downward-moving air as

$$\frac{A_D}{X_H^2} = \gamma\left(\frac{h_{\mathrm{enc}}}{L_0}\right)\left(\frac{X_P}{X_H}\right)\left(\frac{X_H}{L_0}\right)^{-2/3}, \quad (13)$$

where γ is a constant that depends on the heterogeneity amplitude $B_{0\mathrm{NP}}/B_0$, the parameter that we did not use so far. The ratio A_D/X_H^2 can now serve as a scaled time axis during the mesoscale state, where every simulation that shares the same $B_{0\mathrm{NP}}/B_0$, and thus has its own value of γ, has unique values of the ratio for its peak $(h_{\mathrm{enc}}/X_H)_P$ and transition $(h_{\mathrm{enc}}/X_H)_T$. After the sharp transition to the microscale state, the scaling law is no longer valid.

2) CHARACTERISTIC VELOCITY SCALES

The second scaling to be developed is that of the vertically integrated KE. In contrast with the scaling of the time evolution, which is mainly driven by the organization in the downward flow, the KE depends strongly on the upward velocities, since these are very energetic (Fig. 8). In this scaling, we are only considering the cases with no flux in between the patches. We have learned from Fig. 5a that all these cases reach the same value of KE in the optimal state and that they develop toward the same constant normalized KE in the intermediate state before the transition to the microscale regime. Therefore, we base this scaling on the parameter X_P/X_H only. Furthermore, we assume that the variance in the downward-moving air is a function of the KE generated over the patch such that the patch surface buoyancy flux B_{0P} defines the energy input.

To find a velocity scale w_P that is valid over the patches, we formulate a general expression:

$$w_P^2 = \beta w_{\mathrm{enc}}^2, \quad (14)$$

where β is a parameter to be found. In case this velocity scale resembles that of the horizontally homogeneous CBL [Eq. (7)], where the local surface buoyancy flux defines the strength of a plume that can accelerate over height h_{enc}, then according to Eq. (7) w_P^2 has to be equal to

$$(B_{0P}h_{\mathrm{enc}})^{2/3} = \left(\frac{X_P}{X_H}\right)^{-4/3} w_{\mathrm{enc}}^2,$$

where we have made use of Eq. (2) to arrive at the right-hand side expression. This suggests that the value of β is $(X_P/X_H)^{-4/3}$. Our results, however, show a weaker dependence of w_P on the surface buoyancy flux of the patch. To achieve the correct scaling for the results in Fig. 7, we have to take

$$\beta \propto \left(\frac{X_P}{X_H}\right)^{-1} \quad (15)$$

such that we can define the velocity scale as

$$w_P^2 = w_{\mathrm{enc}}^2\left(\frac{X_P}{X_H}\right)^{-1}. \quad (16)$$

The most likely explanation for the weaker dependence of the velocity scale on the patch buoyancy flux is that the finite area of the patch does not allow a plume to increase its surface area. Therefore, it remains relatively narrow compared to a plume in a horizontally homogeneous CBL. The effect is that relatively more lateral entrainment takes place, compared to the larger plumes
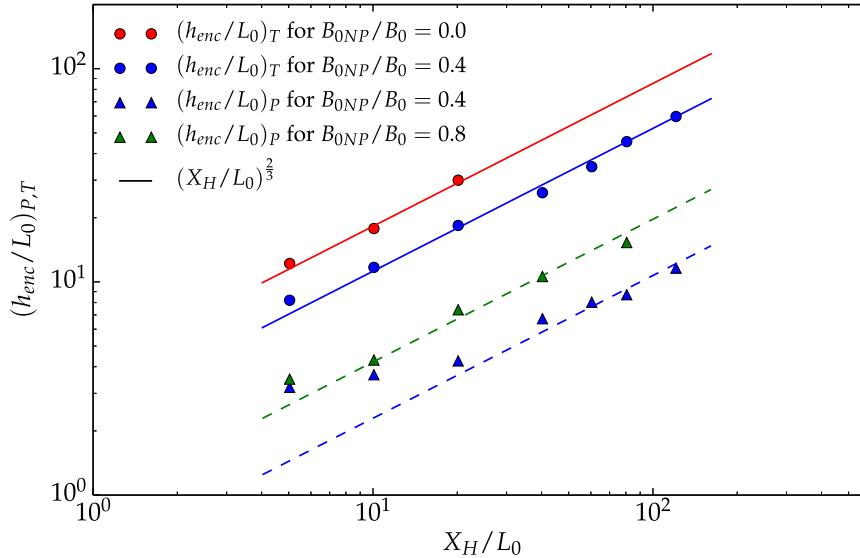
Fig. 10. Timings of the transitions $(h_{enc}/X_H)_T$ and optimal states $(h_{enc}/X_H)_P$ for the simulations in the first experiment (Table 1).

in the horizontally homogeneous CBL, which results in more dissipation and irreversible mixing.

To arrive at the velocity scale w_H that is the proper one for the vertically integrated KE, we have to weight w_P with the fraction of the surface that is covered by patches:

$$w_H^2 = w_P^2 \left(\frac{X_P}{X_H}\right)^2 = w_{enc}^2 \left(\frac{X_P}{X_H}\right). \quad (17)$$

As soon as a flux is added in between the patches, this scaling is no longer valid. We show later that the effects of $B_{0NP}/B_0 > 0$ introduce dependence of the KE on the heterogeneity size but that these effects can be taken into account by the introduction of a correction factor to the previously derived scaling.

b. Demonstration of the scaling laws

1) THE INFLUENCE OF HETEROGENEITY SIZE PARAMETER X_H/L_0

Figure 11 shows the results for simulations sharing a $B_{0NP}/B_0 = 0$ with the new time scaling applied. The scaling law results in collapsing transition times (Fig. 11a) and the magnitudes of KE collapse beyond a scaled time of one, after the system has passed the initial transient.

The height evolution (Fig. 11b) also demonstrates the effective scaling of the transition points, but at the same time, we find that the slopes of the height evolution do not scale under the time scaling. The simulations with a larger heterogeneity size are more constant in time and have a higher CBL height at the moment of transition. This is directly related to the fact that the size of structures in the downward components of the flow grow

relatively faster than the CBL itself. Therefore, the plume is still relatively large in diameter at the moment the transition sets in. The core is thus less diluted than that of the plumes over the smaller patches and therefore is able to reach a greater height. This finding can be corroborated by comparing Figs. 3c and 3d, where both are representing the phase in which the KE is constant under convective scaling, but Fig. 3c, which has the larger value of the heterogeneity size X_H/L_0, has a wider plume with a less diluted core.

To investigate the effect of the scaling on the vertical profiles, we have plotted the horizontal and vertical velocity variances at a scaled time of 1.75 (Figs. 11c,d). Here, it is shown that the scaling collapses the profiles over the entire height, except near the inversion. There is a small shift from vertical to horizontal velocity variance, related to the increasing strength of the inversion with increasing patch size. Our reference simulation of the horizontally homogeneous CBL shows an increasing normalized KE until a scale separation of approximately 25 has been reached between h_{enc} and L_0 (Fig. 5b), which only L2000_0.0 has reached at that point. The increase of horizontal velocity variances during the development toward a self-similar state has also been observed in a growing homogeneously heated CBL (Garcia and Mellado 2014).

2) THE INFLUENCE OF PATCH SIZE PARAMETER X_P/X_H

When applied to the results of the second experiment, the presented scaling results in a very good collapse of both the time evolution of vertically integrated KE and
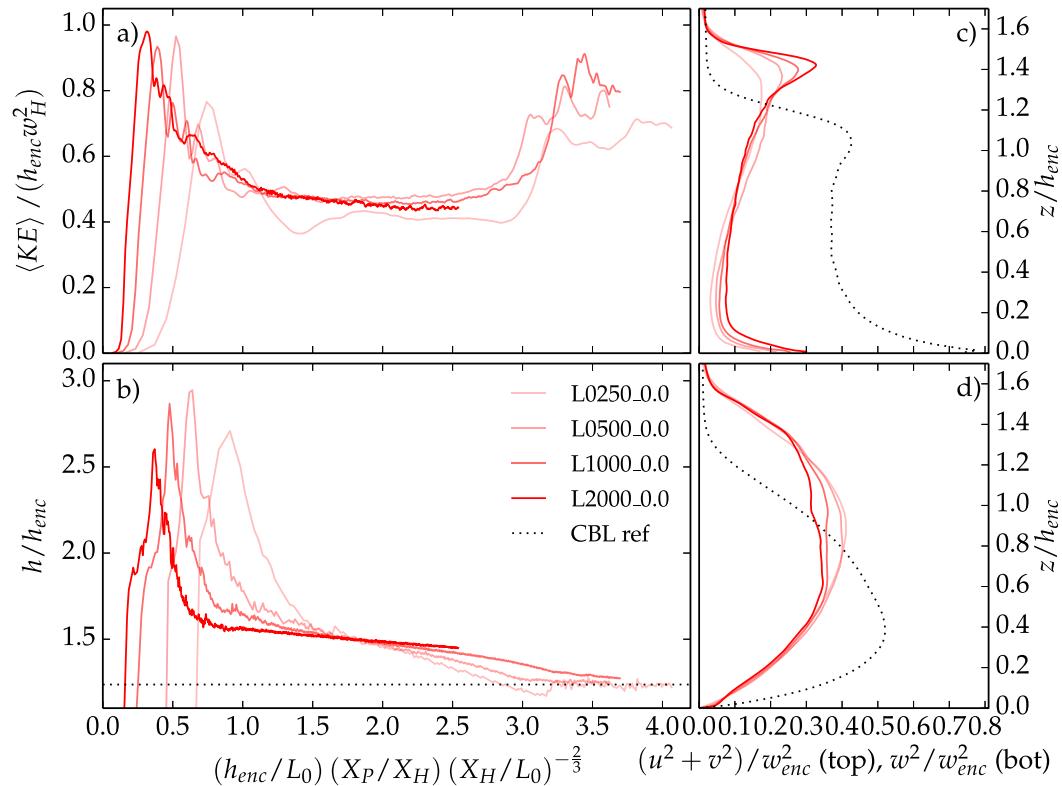
FIG. 11. Time evolutions of the (a) scaled vertically integrated KE and (b) scaled boundary layer height for the simulations with $B_{0L}/B_0 = 0$ from the first experiment. The vertical profiles of (c) horizontal velocity variance and (d) vertical velocity variance are taken at a scaled time $(h_{enc}/L_0)(X_P/X_H)(X_H/L_0)^{-2/3}$ of 1.75.

the CBL height (Fig. 12). All simulations go into transition from the meso- to the microscale regime at the same scaled time of 2.9. Note that simulations D0.125_M and L0250_0.0 share the same nondimensional parameters and therefore go into transition at the same time (see the appendix for a detailed comparison between LES and DNS). The KE reaches a constant value of 0.37 before transition for all three cases. In contrast to the results of the first experiment, the height scaling works very well during the phase in which the KE is constant, where all three simulations develop toward the same linear slope. Simulation D0.125_S reaches this slope at a scaled time of 1.0 and a h/h_{enc} of 1.9, whereas the cases with higher X_P/X_H follow later. They all go into transition at a height that is slightly below the horizontally homogeneous CBL at $1.23\,h/h_{enc}$, indicating that small-scale heterogeneity has less entrainment than the horizontally homogeneous CBL (see section 9).

3) THE INFLUENCE OF THE HETEROGENEITY AMPLITUDE PARAMETER B_{0NP}/B_0

Figure 13 contains the time evolution of the vertically integrated KE and the CBL height for the simulations with a B_{0NP}/B_0 ratio of 0.4. Also for this experiment, the

time of transition from the meso- to the microscale regime well under the developed scaling. Here, the transition occurs at a scaled time value of 1.8, considerably less than the value of 2.9 for the simulations with $B_{0NP}/B_0 = 0$ shown in Fig. 11a. Note that both the KE and the height evolution follow a more complex pattern now than in those simulations.

Figure 6a already showed us the increase in the magnitude of KE of the peak and its delay in time with increasing patch distance X_H/L_0, caused by a secondary circulation. Figure 13a shows that the application of the scaling law for time collapses the moments of the peak in KE and the transition from the meso- to the microscale regime increasingly better for larger heterogeneity sizes. At the moment of transition, the KE levels also converge to the same value, but the KE in the peaks keeps on increasing for larger heterogeneity sizes X_H/L_0. The increase means that the velocity scale w_H [Eq. (17)] does not completely characterize the kinetic energy during the optimal state. This confirms the need for the previously mentioned ad hoc correction factor for the KE, based on nondimensional parameter X_H/L_0, such that magnitudes of KE during the optimal state fall on top of each other under the scaled time axis. We explicitly state
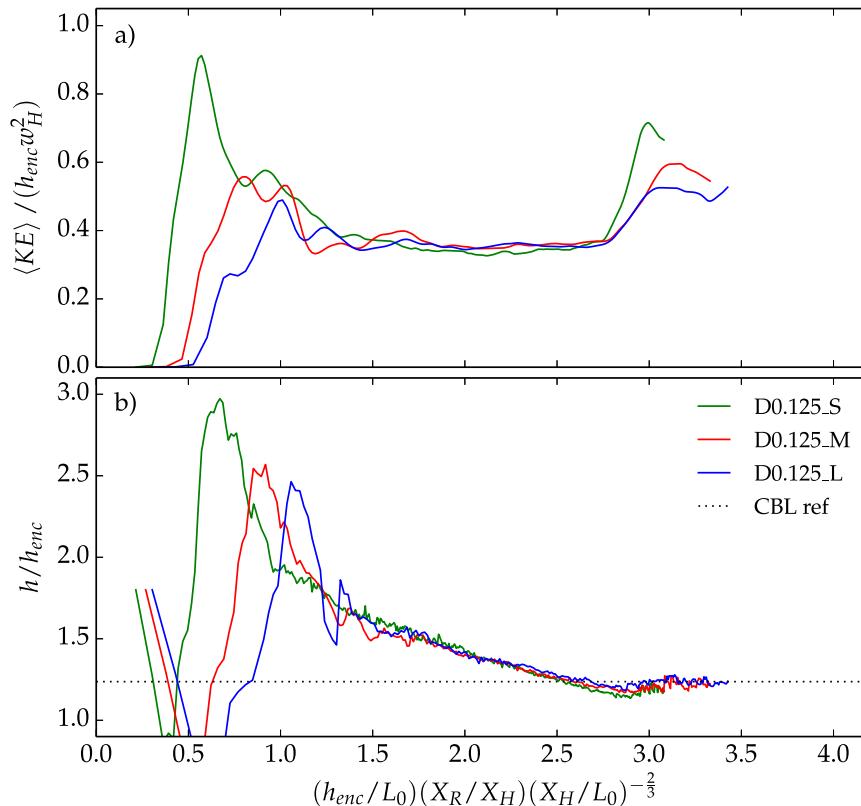
FIG. 12. Time evolutions of (a) the vertically integrated KE and (b) the CBL height for the second experiment.

here that we call this term a correction factor, because we have only simulations with varying heterogeneity amplitude B_{0NP}/B_0 for one value of the patch size X_P/X_H. A complete study is, however, beyond the scope of this paper, as it would introduce a large number of new simulations. The correction factor can be interpreted as an extension of the previously introduced constant β [Eqs. (14) and (15)], which results in a modified velocity scale w'_H:

$$w'^2_H = w^2_H \left(\frac{X_H}{L_0}\right)^{\chi}. \qquad (18)$$

The exponent χ equals zero in case B_{0NP} equals zero and takes a small value of $1/5$ when $B_{0NP} > 0$. The correction factor varies between 1.17 and 1.6 for the simulations in Fig. 13 and is required to take into account the temporary enhancement of the KE due to secondary circulations.

We conclude from Fig. 13b that as soon as the enhancement by the circulation has vanished, the correction is no longer required. This moment corresponds to the moment at which the system arrives at the constant KE line, which we found in Fig. 6a. For instance, simulation

L4000_0.4 reaches this line at h_{enc}/L_0 of 33. Therefore, it departs from the scaling at $(h_{enc}/L_0)(X_P/X_H)(X_H/L_0)^{-2/3}$ equal to 1.25 (Fig. 13b) and returns to the state where the vertically integrated KE values scale without the need for a correction factor.

The time evolution of the CBL height is also influenced by the secondary circulation in the optimal state. During the period at which the secondary circulation is present, there is a suppression of the CBL height that is not found in the experiments without flux in between the patches (Fig. 11). The reason is that simulations with a larger heterogeneity size reach the optimal state at a lower ratio of h_{enc}/X_H (or a higher ratio of X_H/h, see Table 3). Therefore, the aspect ratio (width to height) of the circulation is higher, which results in stronger horizontal motions near the surface. These statements are supported by the vertical profiles of the variances shown in Figs. 13d–f, which depict that the horizontal velocity variance is increasing. A potential implication of the enhanced horizontal motions is that there is stronger mixing over the patch surface, where less-buoyant air that originates from the surroundings of the plume is being mixed into the plume. Therefore, the plumes get less buoyant, resulting in reduced vertical velocity
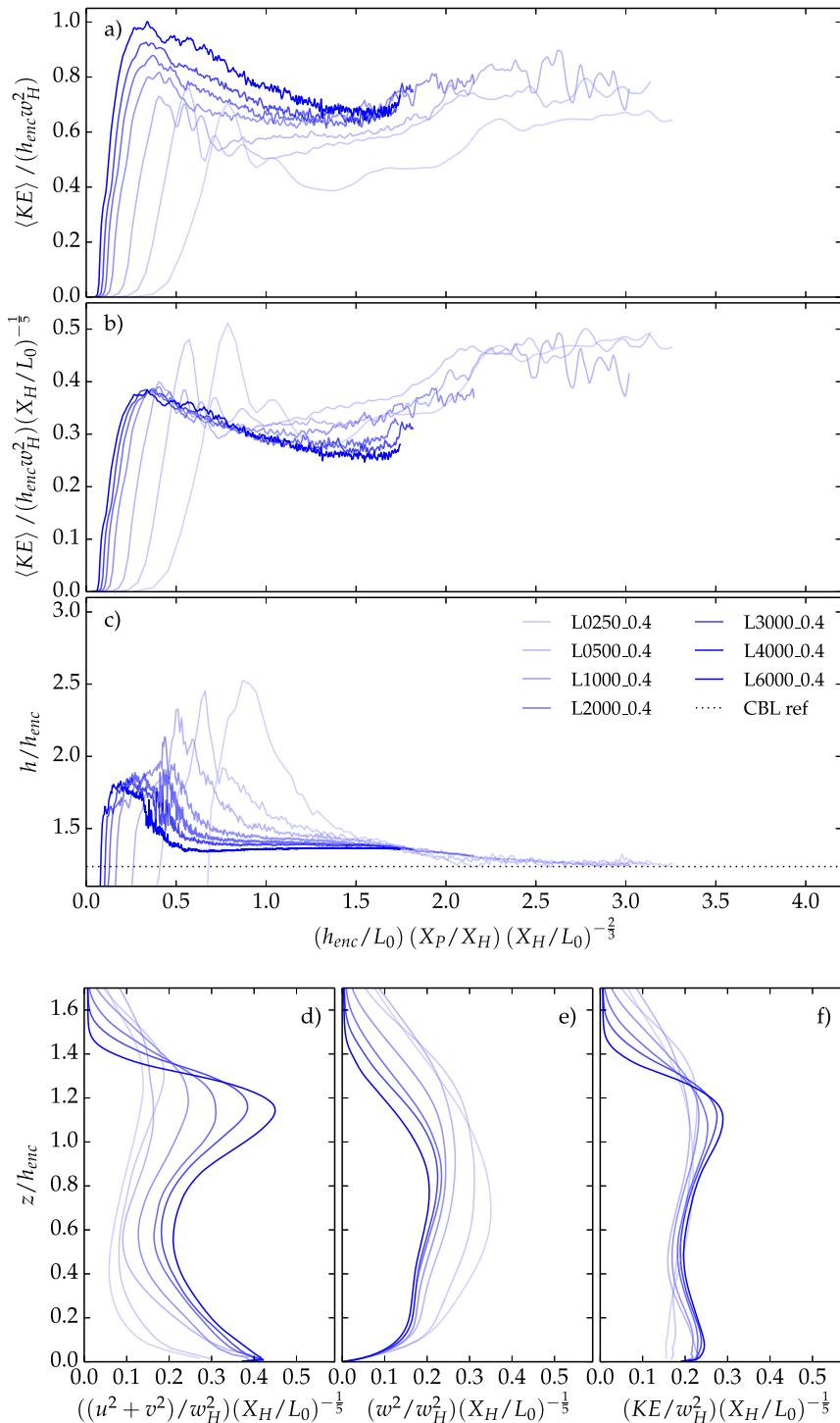
FIG. 13. Time evolutions of the scaled vertically integrated KE (a) without and (b) with correction factor applied and (c) CBL height. The vertical profiles of (d) horizontal velocity variance, (e) vertical velocity variance, and (f) turbulent kinetic energy taken for each simulation with a B_{0NP}/B_0 ratio of 0.4 and at a scaled time value $(h_{enc}/L_0)(X_P/X_H)(X_H/L_0)^{-2/3}$ of 0.75.

variance and a lower scaled CBL height. As soon as the secondary circulations have decayed, the scaled height of the CBL rises slightly.

The vertical profiles of the velocity variances (Figs. 13d,e), show that under application of the correction factor both the horizontal and vertical velocity variances collapse near the surface, where a strong horizontal component of the secondary circulation is present. The vertical profiles of the total KE (Fig. 13f) collapse over the entire height of the CBL, thereby showing that the correction works well.

To further demonstrate the proposed correction factor, we present the unscaled and scaled time evolution of the vertically integrated KE for all simulations with a heterogeneity amplitude described by $B_{0NP}/B_0 = 0.8$ (Fig. 14). These simulations show the same behavior as those with a B_{0NP}/B_0 ratio of 0.4, but the effects are less pronounced and the KE evolves very closely to that of the horizontally homogeneous CBL, making it hard to observe the transition. As the amplitude in this case resembles that of the study of Patton et al. (2005; their Fig. 9), the enhancement of KE is also in their range of 20%.

This figure confirms that a reduction in heterogeneity amplitude delays the optimal state and triggers the transition earlier. With respect to the heterogeneity size, the peaks occur progressively later and with a larger magnitude for an increasing patch distance. The L4000_0.8 case reaches its peak after 3.3 h, whereas the L4000_0.4 case needs only 2 h for this. These peaks are however lower than in the other experiment. Nonetheless, the application of the scaling for the KE shows again a collapse for those cases that have enough time separation between the initial transient and the optimal state, thereby strengthening our confidence in the scaling. The underlying mechanisms, however, still need to be better understood.

9. Discussion

In this section, we address two topics that deserve a separate discussion in light of the existing literature on the heterogeneously heated CBL. These are the ratio of the heterogeneity size to the CBL height that defines the optimal state with the strongest secondary circulations and the enhancement or reduction of entrainment by heterogeneity.

a. The conditions of the optimal state

The first issue to be considered is the definition of the optimal state that has been discussed in previous studies (e.g., Avissar and Schmidt 1998; Patton et al. 2005; Esau 2007). In this paper we have shown that the optimal state cannot simply be expressed in terms of a ratio of the

heterogeneity size and the boundary layer height but that it follows a more complex behavior, in which the heterogeneity size and amplitude have a significant effect. To demonstrate that the estimate of the optimal conditions by Patton et al. (2005) can be explained and refined by our results, we particularize our results to typical atmospheric values, using the value of $L_0 \approx 50$ m defined in section 3.

In Fig. 15 the patch size X_H is plotted against the ratios of X_H to h at which the optimal $(X_H/h)_P$ and transition $(X_H/h)_T$ occur (see also Table 3). Here, we have extrapolated our results to larger heterogeneity sizes in order to make the comparison with the previous studies. Patton et al. (2005) proposed a $(X_H/h)_P$ ratio of 4–9 times the CBL height, which is indicated in the figure. We find that our simulations with the weak amplitude $B_{0NP}/B_0 = 0.8$ have their optimal-state $(X_H/h_{enc})_P$ below the range that Patton et al. (2005) suggested, whereas the stronger-amplitude $B_{0NP}/B_0 = 0.4$ simulations are at the high end of the range that Patton et al. (2005) specified, having a ratio larger than $9(X_H/h)$ for heterogeneity sizes beyond 6 km. If we extrapolate our results to larger heterogeneity sizes, we find that the ratio of the optimal-state $(X_H/h)_P$ increases only marginally and that the size at which the optimal state occurs is mostly a function of heterogeneity amplitude.

The line that extrapolates the measured transition points $(X_H/L_0)_T$ shows little variation beyond a heterogeneity size $X_H \approx 3$ km. It shows that transition occurs when the ratio of the heterogeneity size to the CBL height (X_H/h) is between 1 and 2, depending on the heterogeneity amplitude. In the low end of this range, the transition, therefore, could happen during daytime, but the chances become smaller as the heterogeneity size X_H increases, as we have shown in our results.

To show the sensitivity to the surface buoyancy flux, we have added the lines that correspond to a doubling of the flux to Fig. 15. We find that the optimal state and especially the transition from the meso- to the microscale regime are approximately insensitive to the mean flux and thus mostly depend on the heterogeneity properties.

Two of our most important results, therefore, provide explanations for the large spread between previous studies: First, the influence of heterogeneity size is such that optimal state and transition do not scale under a fixed ratio of X_H/h. Second, the heterogeneity amplitude has a large influence on the time of occurrence of these states.

b. The enhancement of the entrainment rate

Second, a long-standing debate is the question of whether the presence of the circulations in the mesoscale regime enhances the entrainment rate or not. Avissar
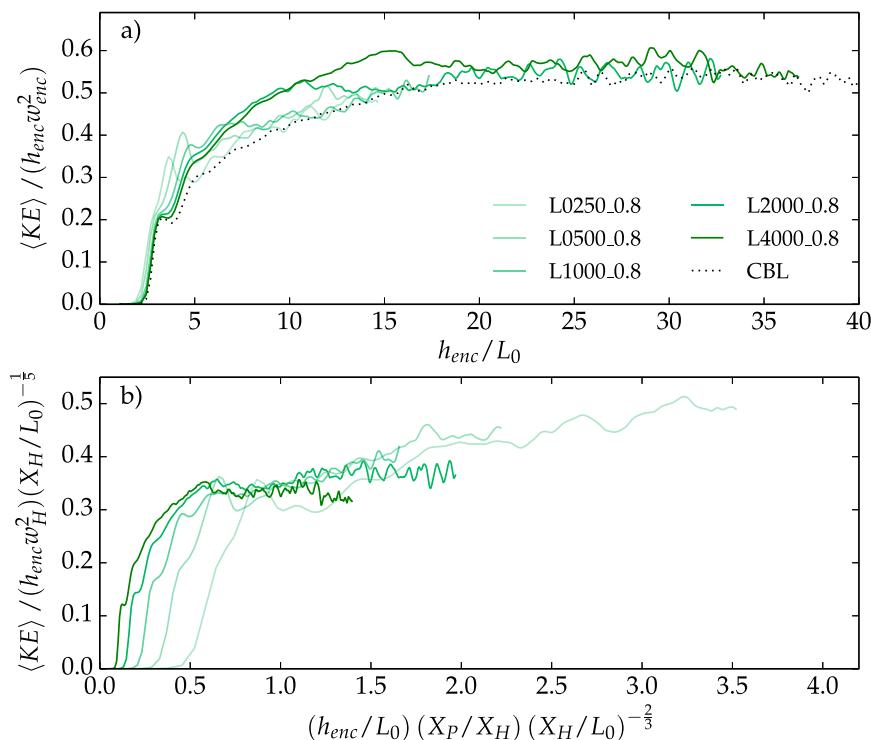
FIG. 14. Time evolutions of (a) the vertically integrated KE and (b) the scaled vertically integrated KE for the simulations from the first experiment with a B_{0L}/B_0 of 0.8.

and Schmidt (1998) found enhanced entrainment over a wide range of heterogeneity sizes and amplitudes, but their resolution was in the range for which Sullivan and Patton (2011) found a strong sensitivity of boundary layer growth to resolution. The study of Patton et al. (2005) claims a minimal influence of heterogeneity on entrainment and shows a small decrease of entrainment for small-scale heterogeneity ($X_H < 4h$) and a slight enhancement for larger heterogeneity sizes ($4h < X_H < 15h$). In contrast, Ouwersloot et al. (2011) found a decrease in entrainment for cases with a small heterogeneity amplitude and an increase in entrainment for a large amplitude when the heterogeneity size is in the order of the CBL height. The most recent study on the issue (Sühring et al. 2014) confirms many of the results of Ouwersloot et al. (2011) using a more detailed analysis of the inversion layer.

Our current result shows that, during the mesoscale regime, all of our simulations have boundary layer heights that exceed those of the homogeneously heated CBL. Since we use the encroachment scaling, a zero slope indicates growth proportional to the horizontally homogeneous CBL, whereas a positive slope indicates faster growth and a negative slope vice versa. In all of our simulations we experience a phase of faster growth toward the optimal state and a reduced growth

afterward. The fact that our results do not scale under the X_H/h ratio might explain the disagreement among Sühring et al. (2014) and Patton et al. (2005) on the X_H/h ratio of maximum entrainment. An additional complication is the complex evolution of the CBL height found in Fig. 13. In section 6 we show that the mixing induced by the heterogeneous circulation enforces a minimum in the CBL height for cases with a nonzero B_{0NP}.

The interpretation of our results and the contradiction among the previous studies is strongly influenced by the problematic determination of the CBL height under heterogeneous conditions, due to large spatial CBL height variations (van Heerwaarden and Vilà-Guerau de Arellano 2008; Ouwersloot et al. 2011; Sühring et al. 2014). In addition to these studies, we have an extra source of information: namely, the state of the system after transition. This state provides a good measure of the time-integrated entrainment induced by secondary circulations. We find that after entering the microscale regime, many of the simulations still need time to converge back to the CBL line, indicating they had a different time-integrated entrainment than the horizontally homogeneous CBL during the mesoscale regime. The return to the line that represents the horizontally homogeneous CBL eventually always happen, because as time progresses, the heat entrained during the mesoscale
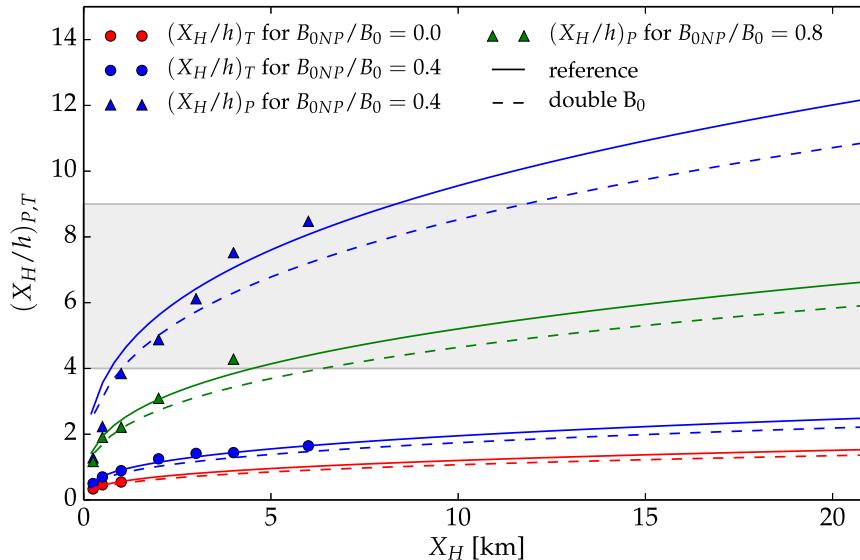
FIG. 15. The link between the absolute heterogeneity size and the ratio between X_H and h at which the transition occurs for the simulations in the first experiment. The colors correspond to those of the time evolutions in Figs. 5, 6, 11, 13, and 14. The gray shaded region marks the range that Patton et al. (2005) specified for the strongest secondary circulations.

state becomes negligible compared to what has been entrained afterward.

Our experiments show that some of the simulations with small patches, such as the L0250_20 (Fig. 5) and all simulations in the second experiment (Fig. 7) have a CBL height lower than the horizontally homogeneous CBL around transition. What those cases have in common is that the initial height of the plumes exceeds the patch size. The simulations with the larger patch sizes (Figs. 5 and 6), where the patches are initially larger than the plume height, have a larger height than the horizontally homogeneous CBL after transition and need a considerably longer time to return to the reference line. With our new measure, we can thus confirm the conclusions of Ouwersloot et al. (2011) and Sühring et al. (2014) and, in addition, explain why there is disagreement on the exact size among the previous studies.

10. Conclusions

In this paper, we have studied the time evolution of the heterogeneously heated convective boundary layer (CBL) in a linearly stratified atmosphere by means of large-eddy simulations (LES) and direct numerical simulations (DNS). Within each simulation, we cover the development from the so-called mesoscale regime, in which strong secondary circulations can develop, to the microscale regime, in which the horizontally homogeneous CBL is recovered. By doing so, we can observe in each simulation the formation of a peak in vertically integrated kinetic energy (KE) that represents

the "optimal" heterogeneity size at which the CBL has the strongest secondary circulations and the subsequent development toward the transition to the microscale regime.

The main findings are the following:

- The optimal state and the transition to a horizontally homogeneous CBL do not occur at a unique ratio of the heterogeneity size X_H and the CBL height h but at larger ratios of X_H/h for larger heterogeneity sizes. Larger heterogeneity sizes reach, therefore, their optimal state at a higher aspect ratio (heterogeneity size to CBL height). This is caused by the development of structures in the downward-moving air that grow faster than the CBL itself. In the mesoscale regime, the downward-moving air decouples from the individual plumes and organizes itself in constantly growing structures that eventually break down the organization imposed by the heterogeneous heating.

- The state of the system can be expressed in a nondimensional variable $(h_{enc}/L_0)(X_P/X_H)(X_H/L_0)^{-2/3}$ This variable relates the boundary layer height h, expressed in terms of the encroachment height h_{enc}, to the heterogeneity size X_H and the patch size X_P (Fig. 1) using the reference Ozmidov length of the CBL $L_0 \equiv (B_0/N^3)^{1/2}$ as a scaling variable (B_0 is the mean surface buoyancy flux and N^2 the stratification). This scaling takes into account the heterogeneity size X_H properly such that the scaled time instant of optimal state and transition is unmodified if the heterogeneity size is changed.
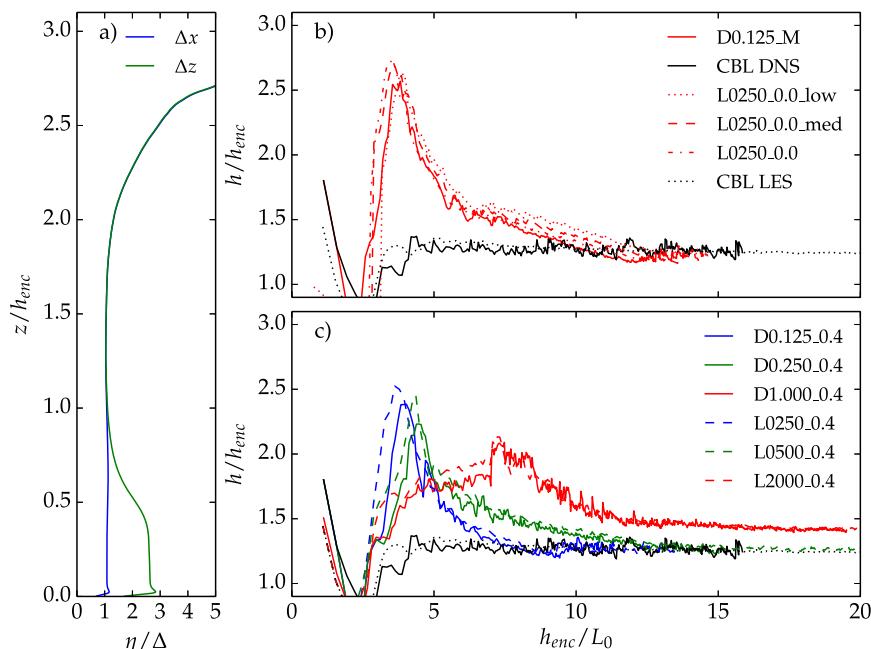
FIG. A1. (a) Ratio of the Kolmogorov length η, calculated following $\eta \equiv (\nu^3/\epsilon)^{1/4}$, to the horizontal ($\Delta x$) and vertical ($\Delta z$) grid spacing during the peak in KE in simulation D0.125_M; time evolution of the scaled boundary layer height (b) for a resolution study for LES and (c) for a comparison of multiple cases between DNS and LES.

- For a given mean surface buoyancy flux, an increase in the heterogeneity amplitude results in an earlier optimal state and delays the transition.
- A reduction of the patch size combined with an increase of the patch heat flux such that the total energy input remains the same results in later transitions from the meso- to the microscale regime and a lower vertically integrated kinetic energy in the mesoscale regime.
- Heterogeneity sizes smaller than or comparable to the initial height of the CBL reduce the entrainment flux of buoyancy, whereas larger heterogeneity sizes that exceed the initial size of the plumes appear to enhance entrainment.

To conclude, our findings improve our understanding of a large part of the parameter space that defines an idealized case of heterogeneous heating: the one without a large-scale forcing. There are three logical extensions to this study. The first is to include a large-scale pressure gradient that brings the effects of wind into the picture. This large-scale forcing can easily be included in the parameter space discussed in section 2b. A second extension would be the introduction of an interactive land surface scheme. Kustas and Albertson (2003) show the existence of feedback mechanisms that try to regulate the area-averaged flux, whereas Patton et al. (2005) show that the maximum fluxes are shifted toward the patch

edges because of the strong circulations. The third and last extension, as already mentioned in the introduction, is toward more complex heterogeneity geometry. Here, we suggest that the heterogeneities should be no longer defined by the heterogeneity size and patch size, but instead by length scales that describe the spectral properties of the heterogeneity. Here, the challenge lies in defining a minimum number of parameters that can adequately describe an arbitrary heterogeneity in order to allow for parameterization. We believe that our framework provides a solid basis for doing so and therefore might open opportunities to further unify the findings of previous studies on the subject.

APPENDIX

Comparison of DNS and LES

In this appendix, we present a short validation of our simulation setup. First, Fig. A1a shows the ratio of the

Kolmogorov length η to the grid spacing during the peak in CBL height and KE in the DNS case D0.125_M (see Fig. 5). The ratio of unity indicates that the flow is very well resolved (Moin and Mahesh 1998).

Second, we have used this case as a reference and have compared it against case L0250_0.0. We have repeated this case at coarser resolution: 1.5 times the grid spacing (L0250_0.0_med) and twice the grid spacing (L0250_0.0_low). Figure A1b shows clearly that the LES results converge toward that of the DNS for increasing resolution. This finding leads to important conclusions: the LES and DNS converge to the same solution; thus, the employed LES resolution is fine enough, and the Reynolds number of the DNS is high enough.

Last, Fig. A1c shows that for a series of experiments the height evolution of the LES and DNS closely follow each other, strengthening the confidence in the reliability of both DNS and LES for this study.

REFERENCES

Ahlers, G., S. Grossmann, and D. Lohse, 2009: Heat transfer and large scale dynamics in turbulent Rayleigh–Bénard convection. *Rev. Mod. Phys.,* **81,** 503–537, doi:10.1103/RevModPhys.81.503.

Albertson, J. D., and M. B. Parlange, 1999: Natural integration of scalar fluxes from complex terrain. *Adv. Water Resour.,* **23,** 239–252, doi:10.1016/S0309-1708(99)00011-1.

Avissar, R., and T. Schmidt, 1998: An evaluation of the scale at which ground-surface heat flux patchiness affects the convective boundary layer using large-eddy simulations. *J. Atmos. Sci.,* **55,** 2666–2689, doi:10.1175/1520-0469(1998)055<2666:AEOTSA>2.0.CO;2.

Baines, W. D., and J. S. Turner, 1969: Turbulent buoyant convection from a source in a confined region. *J. Fluid Mech.,* **37,** 51–80, doi:10.1017/S0022112069000413.

Bou-Zeid, E., C. Meneveau, and M. Parlange, 2005: A scale-dependent Lagrangian dynamic model for large eddy simulation of complex turbulent flows. *Phys. Fluids,* **17,** 025105, doi:10.1063/1.1839152.

Brasseur, J. G., and T. Wei, 2010: Designing large-eddy simulation of the turbulent boundary layer to capture law-of-the-wall scaling. *Phys. Fluids,* **22,** 021303, doi:10.1063/1.3319073.

Cardoso, S. S. S., and A. W. Woods, 1993: Mixing by a turbulent plume in a confined stratified region. *J. Fluid Mech.,* **250,** 277–305, doi:10.1017/S0022112093001466.

Conzemius, R. J., and E. Fedorovich, 2006: Dynamics of sheared convective boundary layer entrainment. Part I: Methodological background and large-eddy simulations. *J. Atmos. Sci.,* **63,** 1151–1178, doi:10.1175/JAS3691.1.

Courault, D., P. Drobinski, Y. Brunet, P. Lacarrere, and C. Talbot, 2007: Impact of surface heterogeneity on a buoyancy-driven convective boundary layer in light winds. *Bound.-Layer Meteor.,* **124,** 383–403, doi:10.1007/s10546-007-9172-y.

Deardorff, J. W., 1970: Convective velocity and temperature scales for the unstable planetary boundary layer and for Rayleigh convection. *J. Atmos. Sci.,* **27,** 1211–1213, doi:10.1175/1520-0469(1970)027<1211:CVATSF>2.0.CO;2.

Esau, I. N., 2007: Amplification of turbulent exchange over wide Arctic leads: Large-eddy simulation study. *J. Geophys. Res.,* **112,** D08109, doi:10.1029/2006JD007225.

Fedorovich, E., 1995: Modeling the atmospheric convective boundary layer within a zero-order jump approach: An extended theoretical framework. *J. Appl. Meteor.,* **34,** 1916–1928, doi:10.1175/1520-0450(1995)034<1916:MTACBL>2.0.CO;2.

Garcia, J. R., and J. P. Mellado, 2014: The two-layer structure of the entrainment zone in the convective boundary layer. *J. Atmos. Sci.,* **71,** 1935–1955, doi:10.1175/JAS-D-13-0148.1.

Górska, M., J. Vilà-Guerau de Arellano, M. LeMone, and C. C. van Heerwaarden, 2008: Mean and flux horizontal variability of virtual potential temperature, moisture, and carbon dioxide: Aircraft observations and LES study. *Mon. Wea. Rev.,* **136,** 4435–4451, doi:10.1175/2008MWR2230.1.

Heus, T., and Coauthors, 2010: Formulation of the Dutch Atmospheric Large-Eddy Simulation (DALES) and overview of its applications. *Geosci. Model Dev.,* **3,** 415–444, doi:10.5194/gmd-3-415-2010.

Huang, H.-Y., and S. A. Margulis, 2009: On the impact of surface heterogeneity on a realistic convective boundary layer. *Water Resour. Res.,* **45,** W04425, doi:10.1029/2008WR007175.

——, and ——, 2010: Evaluation of a fully coupled large-eddy simulation–land surface model and its diagnosis of land-atmosphere feedbacks. *Water Resour. Res.,* **46,** W06512, doi:10.1029/2009WR008232.

Jonker, H. J. J., P. G. Duynkerke, and J. W. M. Cuijpers, 1999: Mesoscale fluctuations in scalars generated by boundary layer convection. *J. Atmos. Sci.,* **56,** 801–808, doi:10.1175/1520-0469(1999)056<0801:MFISGB>2.0.CO;2.

Kaimal, J. C., J. C. Wyngaard, D. A. Haugen, O. R. Coté, Y. Izumi, S. J. Caughey, and C. J. Readings, 1976: Turbulence structure in the convective boundary layer. *J. Atmos. Sci.,* **33,** 2152–2169, doi:10.1175/1520-0469(1976)033<2152:TSITCB>2.0.CO;2.

Kang, S.-L., 2009: Temporal oscillations in the convective boundary layer forced by mesoscale surface heat-flux variations. *Bound.-Layer Meteor.,* **132,** 59–81, doi:10.1007/s10546-009-9391-5.

——, and D. Lenschow, 2014: Temporal evolution of low-level winds induced by two-dimensional mesoscale surface heat-flux heterogeneity. *Bound.-Layer Meteor.,* **151,** 501–529, doi:10.1007/s10546-014-9912-8.

——, K. J. Davis, and M. LeMone, 2007: Observations of the ABL structures over a heterogeneous land surface during IHOP_2002. *J. Hydrometeor.,* **8,** 221–244, doi:10.1175/JHM567.1.

Kustas, W. P., and J. D. Albertson, 2003: Effects of surface temperature contrast on land-atmosphere exchange: A case study from Monsoon 90. *Water Resour. Res.,* **39,** 1159, doi:10.1029/2001WR001226.

Lenschow, D. H., and B. B. Stankov, 1986: Length scales in the convective boundary layer. *J. Atmos. Sci.,* **43,** 1198–1209, doi:10.1175/1520-0469(1986)043<1198:LSITCB>2.0.CO;2.

Letzel, M. O., and S. Raasch, 2003: Large-eddy simulation of thermally induced oscillations in the convective boundary layer. *J. Atmos. Sci.,* **60,** 2328–2341, doi:10.1175/1520-0469(2003)060<2328:LESOTI>2.0.CO;2.

Mahrt, L., 2000: Surface heterogeneity and vertical structure of the boundary layer. *Bound.-Layer Meteor.,* **96,** 33–62, doi:10.1023/A:1002482332477.

Maronga, B., and S. Raasch, 2013: Large-eddy simulations of surface heterogeneity effects on the convective boundary layer during the LITFASS-2003 experiment. *Bound.-Layer Meteor.,* **146,** 17–44, doi:10.1007/s10546-012-9748-z.

Mellado, J. P., 2012: Direct numerical simulation of free convection over a heated plate. *J. Fluid Mech.,* **712,** 418–450, doi:10.1017/jfm.2012.428.

Moin, P., and K. Mahesh, 1998: Direct numerical simulation: A tool in turbulence research. *Annu. Rev. Fluid Mech.,* **30,** 539–578, doi:10.1146/annurev.fluid.30.1.539.

Morinishi, Y., T. S. Lund, O. V. Vasilyev, and P. Moin, 1998: Fully conservative higher order finite difference schemes for incompressible flow. *J. Comput. Phys.,* **143,** 90–124, doi:10.1006/jcph.1998.5962.

Morton, B. R., G. Taylor, and J. S. Turner, 1956: Turbulent gravitational convection from maintained and instantaneous sources. *Proc. Roy. Soc. London,* **234A,** 1–23, doi:10.1098/rspa.1956.0011.

Ouwersloot, H. G., J. Vilà-Guerau de Arellano, C. C. van Heerwaarden, L. N. Ganzeveld, M. C. Krol, and J. Lelieveld, 2011: On the segregation of chemical species in a clear convective boundary layer over heterogeneous land surfaces. *Atmos. Chem. Phys.,* **11,** 10 681–10 704, doi:10.5194/acp-11-10681-2011.

Patton, E. G., P. P. Sullivan, and C.-H. Moeng, 2005: The influence of idealized heterogeneity on wet and dry planetary boundary layers coupled to the land surface. *J. Atmos. Sci.,* **62,** 2078–2097, doi:10.1175/JAS3465.1.

Piomelli, U., and E. Balaras, 2002: Wall-layer models for large-eddy simulations. *Annu. Rev. Fluid Mech.,* **34,** 349–374, doi:10.1146/annurev.fluid.34.082901.144919.

Prueger, J. H., and Coauthors, 2012: Patch scale turbulence over dryland and irrigated surfaces in a semi-arid landscape under advective conditions during BEAREX08. *Adv. Water Resour.,* **50,** 106–119, doi:10.1016/j.advwatres.2012.07.014.

Raasch, S., and G. Harbusch, 2001: An analysis of secondary circulations and their effects caused by small-scale surface inhomogeneities using large-eddy simulation. *Bound.-Layer Meteor.,* **101,** 31–59, doi:10.1023/A:1019297504109.

Shao, Y., S. Liu, J. H. Schween, and S. Crewell, 2013: Large-eddy atmosphere–land-surface modelling over heterogeneous surfaces: Model development and comparison with measurements. *Bound.-Layer Meteor.,* **148,** 333–356, doi:10.1007/s10546-013-9823-0.

Smyth, W. D., and J. N. Moum, 2000: Length scales of turbulence in stably stratified mixing layers. *Phys. Fluids,* **12,** 1327–1342, doi:10.1063/1.870385.

Sühring, M., and S. Raasch, 2013: Heterogeneity-induced heat-flux patterns in the convective boundary layer: Can they be detected from observations and is there a blending height?—A large-eddy simulation study for the LITFASS-2003 experiment. *Bound.-Layer Meteor.,* **148,** 309–331, doi:10.1007/s10546-013-9822-1.

——, B. Maronga, F. Herbort, and S. Raasch, 2014: On the effect of surface heat-flux heterogeneities on the mixed-layer-top entrainment. *Bound.-Layer Meteor.,* **151,** 531–556, doi:10.1007/s10546-014-9913-7.

Sullivan, P. P., and E. G. Patton, 2011: The effect of mesh resolution on convective boundary layer statistics and structures generated by large-eddy simulation. *J. Atmos. Sci.,* **68,** 2395–2415, doi:10.1175/JAS-D-10-05010.1.

Tennekes, H., 1973: A model for the dynamics of the inversion above a convective boundary layer. *J. Atmos. Sci.,* **30,** 558–567, doi:10.1175/1520-0469(1973)030<0558:AMFTDO>2.0.CO;2.

van Heerwaarden, C. C., and J. Vilà-Guerau de Arellano, 2008: Relative humidity as an indicator for cloud formation over heterogeneous land surfaces. *J. Atmos. Sci.,* **65,** 3263–3277, doi:10.1175/2008JAS2591.1.

Vasilyev, O. V., 2000: High order finite difference schemes on nonuniform meshes with good conservation properties. *J. Comput. Phys.,* **157,** 746–761, doi:10.1006/jcph.1999.6398.

Williamson, J. H., 1980: Low-storage Runge–Kutta schemes. *J. Comput. Phys.,* **35,** 48–56, doi:10.1016/0021-9991(80)90033-9.

Yan, Z. H., 2007: Large-eddy simulations of a turbulent thermal plume. *Heat Mass Transfer,* **43,** 503–512, doi:10.1007/s00231-006-0127-5.